STAFF SUMMARY SHEET

	TO	ACTION	SIGNATURE (Surname), GRADE AND DATE		TO	ACTION	SIGNATURE (Surname), GRADE AND DATE
1	DFEM	coord	Rhymer LtCol (see sticky) 6 May 2014	6			
2	DFER	approve	SULTI, AD-22, 7 May 14	7			
3	DFEM/ CAStLE	action		8			
4				9			
5				10			

SURNAME OF ACTION OFFICER AND GRADE	SYMBOL	PHONE	TYPIST'S INITIALS	SUSPENSE DATE
Dr. James Greer, Jr.	DFEM/CAStLE	333-3618	lgm	20140501

SUBJECT		DATE
Clearance for Material for Public Release	USAFA-DF-PA- 308	20140509

SUMMARY

1. PURPOSE. To provide security and policy review on the document at Tab 1 prior to release to the public.

2. BACKGROUND.
Authors: J.T. Burns, R.P. Gangloff, J. Ai, and J.L Jones University of Virginia and R.W. Bush and Y. Lee United States Air Force Academy

Title: Effect of Water Vapor Pressure on Fatigue Crack Growth in Al-Zn-Cu-Mg Alloy Over Wide-range Stress Intensity Factor Loading

Circle one: Abstract Tech Report (Journal Article) Speech Paper Presentation Poster Thesis/Dissertation Book Other: _____

Check all that apply (For Communications Purposes):
[] CRADA (Cooperative Research and Development Agreement) exists
[] Photo/ Video Opportunities [] STEM-outreach Related [] New Invention/ Discovery/ Patent

Description: Special Issue (SI) of Engineering Fracture Mechanics: Corrosion Fatigue

Previous Clearance information: NA

Recommended Distribution Statement: Distribution A: approved for public release, distribution unlimited

3. DISCUSSION. This research was performed under the sponsorship of the DoD Office of Corrosion Policy and Oversight and the Center for Aircraft Structural Life Extension (CAStLE)

4. RECOMMENDATION: Department Head or designee review as subject matter expert. DFER review for policy and security and provide public release clearance.

Kevin J. LaRochelle, LtCol
Deputy, CAStLE

2 Tabs
1. Article
2. Figures

Effect of Water Vapor Pressure on Fatigue Crack Growth in Al-Zn-Cu-Mg Alloy Over Wide-range Stress Intensity Factor Loading

J.T. Burns[1], R.W. Bush[2], J. Ai[1], J.L Jones[1], Yongwon Lee[1,2], R.P. Gangloff[1]

[1] University of Virginia, Charlottesville, VA 22904
[2] United States Air Force Academy, USAF Academy, CO 80841

Abstract

The objective of this research is to broaden understanding of the deleterious effect of high purity water vapor on fatigue crack growth rate (da/dN) in aluminum alloy 7075-T651, with focus on the low da/dN regime. Growth rate declines with decreasing water vapor pressure over a very wide range of stress intensity range (ΔK) and maximum stress intensity (K_{max}) levels. Behavior is understood based on the established processes of Knudsen diffusion of water vapor molecules to the occluded crack tip, surface reaction to produce atomic H, H diffusion into the crack tip fracture process zone, and H-plasticity-stress interaction. Growth rate exhibits a novel minimum for intermediate water vapor pressures and low ΔK at both constant R and constant K_{max}. Here, the decline in Stage I rate toward the inert environment threshold transitions to increasing da/dN with further decreases in ΔK and at very low ΔK merges with growth rates typical of high water vapor pressures. With da/dN increase through the minimum, faceted slip band cracking in Stage I transitions to a flat-transgranular mode characteristic of hydrogen embrittlement. The da/dN minimum is explained based on increased water vapor supply to the otherwise occluded crack tip due to the onset of turbulent-convective mixing from Stage I crack asperity contact, thus reigniting hydrogen environment embrittlement which would otherwise not occur at very low water vapor pressures governed by Knudsen diffusion and/or orderly lamellar advection. Low rates of Stage I fatigue cracking, which precede the onset of the da/dN minimum can lead to a false-high threshold stress intensity range for low water vapor pressure environments.

1. Introduction

Fatigue crack propagation (FCP) rate (da/dN) is well described by stress intensity range ($\Delta K = K_{max} - K_{min}$) and maximum stress intensity (K_{max} or $R = K_{min}/K_{max}$) since these parameters control the crack tip plastic strain range and normal stress that govern local damage evolution [1-4]. Environment has an equally important impact on da/dN for structural metals [5-10]. For precipitation hardened aluminum alloys, loading in moist-gaseous environments enhances da/dN relative to crack growth in ultra-high vacuum, with growth rate increase correlated to the ratio of water vapor pressure (P_{H2O}) to loading frequency (f) [6-9, 11]. For this class of alloys, da/dN depends on the interaction of ΔK, K_{max} and P_{H2O}/f; the resulting complex crack growth rate law is central to accurate damage tolerant component prognosis [12-14] and alloy development [15-17]. While stress intensity dependencies of da/dN have been broadly investigated and incorporated in FCP life prediction for over 40 years, the environmental effect has been studied largely from the scientific perspective and not quantitatively incorporated in life prediction [6]. This deficiency can be important for prognosis of the fatigue performance of airframe components that experience inflight loading environments varying from low-temperature (well below 0°C) and low-water vapor pressure at high altitudes to ambient temperature (23°C) and high humidity at low altitudes [18].

Understanding the occluded-crack tip environment, and mechanism(s) of damage evolution, are central to modeling FCP kinetics [6, 7]. Wei and coworkers pioneered understanding of the dependence of da/dN on P_{H2O}/f for FCP in aluminum alloys stressed in pure water vapor at a given ΔK and R, based on the hydrogen environment embrittlement (HEE) perspective [6]. The environmental contribution to da/dN is governed by the time-cycle dependent concentration of atomic hydrogen (H), which is produced on crack tip surfaces from water vapor reaction with Al and perhaps capillary condensation at higher P_{H2O}, and in turn delivered by trap-sensitive diffusion into the crack tip fracture process zone (FPZ). Crack growth kinetics are modeled based on the hypothesis that da/dN is limited by the slowest step in this sequence of mass transport in the occluded crack, crack surface reaction(s), and diffusion of damaging H [6, 19]. The dependence of da/dN on ΔK, K_{max} and P_{H2O}/f reflects the dependence of the rate-controlling process(es) on these variables, as well as on alloy microstructure. Specific models have been developed for Al alloys with da/dN limited by: (a) transport of water vapor molecules from the bulk environment to the occluded crack tip as governed by impeded Knudsen flow such that da/dN

is directly proportional to P_{H2O}/f [20-29], (b) the rate of the Al-H_2O surface reaction to produce a surface layer of adsorbed-atomic H, where da/dN is independent of P_{H2O}/f [20, 21, 27] and (c) H diffusion in the FPZ with da/dN proportional to a complex function of P_{H2O}/f [17, 30-32]. The fundamental mechanism by which H in the FPZ interacts with local plastic strain range and stress is controversial [33, 34], but recent results demonstrate a physical basis for H-assisted damage evolution within the crack tip FPZ [35]. This perspective is adapted in the present study, and the extent of da/dN enhancement due to crack-tip surface oxide/hydroxide formation [36] and enhanced opening plasticity/surface energy reduction [28, 37] is considered in the Discussion.

Investigations of the dependence of da/dN on ΔK, K_{max} and P_{H2O}/f for aerospace aluminum alloys are deficient with regard to breadth. Modern work recognized the importance of controlling water vapor purity and pressure through an ultra-high vacuum (UHV) system which is capable of reducing impurity partial pressures to less than 1 μPa [6, 11, 17, 24, 38-40]. Scientific studies, which focused on the effect of P_{H2O}/f were largely limited to ΔK levels in the mid-Paris regime (above about 6 MPa√m and 4 x 10^{-5} mm/cycle) for Al-Zn-Mg-Cu [10, 11, 24-27, 29, 38, 41, 42], Al-Cu [20, 21], Al-Cu-Mg [10, 11, 17], Al-Cu-Li [17], and Al-Mg [11] alloys. Experimental results have been reported for lower ΔK levels, with da/dN approaching 10^{-7} to 10^{-8} mm/cycle, but the environment was typically restricted to either moist air or UHV [9, 43-46]. In most of these studies, R was low (0.05 to 0.1) so crack surface closure may have impacted measured da/dN versus applied ΔK. For a wide range of ΔK, R impacts: (a) crack closure, (b) transport of water vapor molecules within the fatigue crack [47], and (c) tensile stress-plastic strain range sensitive crack tip damage [2, 4, 35]. These deficiencies were recently addressed for an Al-Zn-Mg-Cu alloy [40], as well as several Al-Cu-Mg/Li alloys [48], and limited results were reported for the P_{H2O}/f dependence of da/dN at high R and low ΔK for Al-Li-Cu and Al-Zn-Mg-Cu alloys in several purified gas environments [39]. Generally, however, systematic measurement and modeling of the effect of environmental exposure on FCP rate is lacking for the lower-Paris to near-threshold regime (da/dN < 10^{-5} mm/cycle). These data are critically important to assess the relevance of rate limited step modeling in the lower growth rate regime, where crack advance is likely discontinuous, as well as to guide fatigue prognosis pertinent to small crack and associated-low stress intensity levels.

As a second limitation, interaction of stress intensity loading protocol and water vapor exposure may impact da/dN, as suggested by recent data [40]. Typical experimental

determinations of the P_{H2O} dependence of da/dN employed rising ΔK at constant R [11, 21, 24, 25, 47] or constant ΔK at constant R [17, 39]. The results of these approaches have not been compared to assess the impact of loading format and history on environment-sensitive da/dN. Moreover, near threshold fatigue crack growth rates are effectively probed by decreasing ΔK loading at either constant R [15] or constant K_{max} [16, 49, 50], but this loading protocol has not been coupled with systematic variation of P_{H2O}/f.

The objective of this research is to characterize and understand the effect of water vapor pressure on FCP kinetics over a wide range of exposure and stress intensity range for an Al-Zn-Mg-Cu alloy. The FCP rate dependence on P_{H2O}/f is systematically established for the near threshold regime via constant ΔK-high R experiments, augmented by decreasing ΔK experiments (ΔK-shed testing) at either constant K_{max} or constant R in order to establish FCP behavior over a wide range of ΔK and ultra-high vacuum system-controlled P_{H2O}/f levels.

2. Experimental Methods

The material studied was 50.8 mm thick 7075-T651 plate taken from a large-scale heat prepared to simulate a typical legacy composition and investigated in an interdisciplinary program on multi-scale modeling for airframe fatigue prognosis [51-53]. The microstructure was peak aged, partially recrystallized and documented elsewhere [54]. The grain size at the plate-center plane is 200 to 1000 μm in the rolling-longitudinal (L) direction, 30 to 300 μm in the width (transverse, T) direction, and 10 to 70 μm in the thickness (S) direction, where most grains were un-recrystallized. The grain size at T/7.3 is 100 to 500 μm in the L direction, 20 to 150 μm in the T direction, and 10 to 40 μm in the S direction due to enhanced recrystallization. Tensile yield and ultimate strengths in the longitudinal direction were 508 and 598 MPa respectively. The plane strain fracture toughness was 33 MPa√m, and conventional FCP data for stressing in moist air were reported [55], each for the L-T crack orientation.

Fatigue crack growth experiments were performed in accordance with ASTM E647, where crack length was calculated from crack mouth opening displacement using compliance [56]. Compact tension (CT) specimens were machined in both the L-T and T-L orientations. L-T oriented specimens were centered between 7.0 to 8.5 mm from the plate surface (T/6 to T/7.3), while the T-L specimens were centered 17 to 25.4 mm from the plate surface (T/3 to T/2).

Specimen width (W) and thickness (B) were 50.8 and 6.35 mm, respectively. The notch depth was 12.7 mm ahead of the load line (a/W = 0.25) and mouth opening was 3 mm. The effect of P_{H2O}/f on da/dN was characterized by two distinct loading formats, each applied at a single loading frequency of 20 Hz. First, growth rates were measured at low-constant ΔK (3.5, 4.5, and 5.5 MPa$\sqrt{m}$) and high-constant R (0.5, 0.5 and 0.65, respectively). At each ΔK level, a single CT specimen (L-T orientation) was used to determine da/dN over a broad range of P_{H2O}/f varying from high to low exposure and with each exposure level held constant during an interval (~1 mm) of growth. Linear regression of crack length versus cycles over this interval yielded da/dN, which was generally constant suggesting steady state growth. Alternately, da/dN was measured for a wide range of ΔK using constant K_{max} (16.5 MPa$\sqrt{m}$) or constant R (0.5) with ΔK decreasing according to $\Delta K=\Delta K_o \exp[C(a-a_o)]$ where ΔK_o = 14.85 MPa$\sqrt{m}$, a_o = 12.7 mm, and C = -0.07 mm^{-1} (constant K_{max}) or -0.08 mm^{-1} (constant R). Loading was begun at R of +0.1 and continued until either the da/dN fell to approximately 5 x 10^{-8} mm/cycle or ΔK reached approximately 2 MPa$\sqrt{m}$. Growth rate was determined at a specific ΔK using a 7-point incremental polynomial curve fit and differentiation [56].

All FCP experiments were conducted in a Cu-gasket-sealed stainless steel UHV chamber. Pure water vapor was introduced from a sealed glass flask containing triply distilled water, via a precision leak valve adjusted so that total pressure was dynamically maintained at a measured level by balanced water vapor input and turbo pumping. Prior to water introduction, the dynamically pumped UHV pressure was 0.25 to 0.50 μPa. A quadruple mass spectrometer confirmed that the measured partial pressure of impurities in the vacuum chamber-contained water vapor was less than 0.013 to 0.025 μPa through all experiments. The measured impurities were a mixture of CO_2 and N_2, neither of which is expected to affect FCP in Al alloys.

3. Results

3.1 Fatigue Crack Growth Kinetics

The influence of fatigue loading protocol on da/dN was first investigated for UHV. The expected two regime da/dN versus ΔK response was observed for 7075-T651 (L-T) subjected to three loading conditions centered on continuously decreasing ΔK, Figure 1. Using the constant K_{max} (16.5 MPa$\sqrt{m}$) experiment as a baseline, increasing K_{max} to 32 MPa$\sqrt{m}$, while starting the

ΔK-shed at the same ΔK, results in higher da/dN values and a lower apparent ΔK_{TH}, as expected due to increasing R at any ΔK. (The high scatter in da/dN is likely due to superposition of constituent-particle based fatigue microvoid formation [57], favored by K_{max} nearly equaling the K_{IC} of 7075-T651 (33 MPa√m) and interacting with ΔK-based cyclic plasticity proximate to particles, as supported by isolated ductile rupture features on the fatigue crack surface). The decreasing ΔK experiment at constant R of 0.5 resulted in a higher threshold compared to the constant K_{max} data sets with R of 0.90 and 0.77, and crossed each constant K_{max} curve at approximately the ΔK level which yielded an R of 0.5. The UHV da/dN vs. ΔK relationships in Figure 1 do not exhibit the novel threshold transition response that was observed for these loading protocols applied to 7075-T651 in various water vapor, as demonstrated by the ensuing results.

Fatigue crack growth rate in 7075-T651 (L-T) depends strongly on $\mathbf{P}_{H2O}/f$ in the low ΔK regime. Figure 2 presents growth rates measured from constant ΔK-constant R loading plotted versus P_{H2O}/f. These rates are steady state and reasonably free of crack closure impact given (a) the relatively high R values (0.5 or 0.65) and (b) exclusion of rates where either compliance non-linearity or crack length dependent da/dN at constant ΔK indicated closure. These da/dN values agree with measured, as well as closure-model compensated da/dN, reported for the same lot of 7075-T651 (L-T) stressed in moist air with an effective P_{H2O}/f of 130-300 Pa-s [55]; see x in Figure 2. Growth rates at ΔK of 3 MPa√m exhibit more than a two order of magnitude increase in da/dN with P_{H2O}/f increasing from 3×10^{-4} to 100 Pa-s for a single CT specimen. The data for ΔK of 4.5 MPa√m show a nearly 3 order of magnitude increase in da/dN as P_{H2O}/f rises from UHV to ~100 Pa-s. The steady state da/dN results in Figure 2 for constant ΔK of 4.5 and 3.0 are consistent with UHV (~2×10^{-8} Pa-s) da/dN in Figure 1 extrapolated toward 10^{-7} mm/cycle and lower, suggesting a threshold ΔK (ΔK_{TH}) which is about 4.5 MPa√m at R of 0.5. The water vapor exposure dependence of da/dN at these two low ΔK levels is consistent with literature results obtained for higher ΔK levels [10, 17, 20, 21, 23-27, 47], where the change in da/dN with rising P_{H2O}/f is smaller (see ΔK = 5.5 MPa√m in Figure 1). The dashed trend lines were not drawn to comply with the specific da/dN values in Figure 2, but rather were transferred from fits to a larger data base for constant R of 0.5 (● in Figure 6 and ■ in Figure 12) and constant K_{max} at R of 0.65 (Δ in Figure 12), as presented in the following sections.

The effect of water vapor exposure on wide-range da/dN versus ΔK, determined by

constant K_{max}-decreasing ΔK loading, is shown in Figure 3 for 7075-T651 (L-T). Above a ΔK of 5 MPa√m ($0.70 > R > 0.10$) da/dN values are essentially equal for very low water vapor exposures from UHV to P_{H2O} of 0.13 Pa (perhaps including 0.26 Pa). The 2.6 Pa data exhibit a limited plateau at ΔK of 10 to 11 MPa√m, indicative of transition from mechanically driven crack growth at higher ΔK to environment-assisted cracking at lower ΔK. For these moderate ΔK levels, a 1000-fold increase in P_{H2O} above 2.6 Pa results in only a 3-fold rise in da/dN. Considering ΔK levels below 5 MPa√m, to as low as 1.8 MPa√m ($0.67 < R < 0.90$), da/dN depends strongly on both ΔK and P_{H2O}. For higher P_{H2O} (2.6 Pa to 2.4 kPa), there is no observable sharp reduction in da/dN toward a threshold for ΔK as low as 1.8 MPa√m. This result is consistent with reported ΔK_{TH} of 1.3 to 1.4 MPa√m (R of 0.90 and 0.70, respectively) [55] for this lot of 7075-T651 (L-T) stressed in moist air with P_{H2O} equaling 1.8 kPa for a typical relative humidity of 60% . In contrast a strong Stage I growth rate response is observed for UHV, suggesting a ΔK_{TH} of 3.8 MPa√m at R of 0.77 and specific to the CT geometry [58, 59]. A novel da/dN versus ΔK relationship is observed for P_{H2O} values of 0.006, 0.053 and 0.13 Pa; that is, da/dN approaches a threshold which parallels the UHV trend, then reverses at a ΔK of 4.1 to 3.9 MPa√m (R of 0.75 to 0.76) such that crack growth rate increases as ΔK decreases. This region is termed the threshold transition. With continued decrease in ΔK, two of these three growth rate curves approaches and merges with data from higher water vapor pressures that did not exhibit this novel minimum in da/dN and did not exhibit a ΔK_{TH}. The minimum da/dN decreases by 26 times with a 22-fold decrease in P_{H2O} from 0.13 to 0.006 Pa.

The dependence of da/dN on ΔK and P_{H2O} for the T-L orientation of 7075-T651 (Figure 4) is essentially identical to that measured for the L-T orientation (Figure 3) under identical constant ΔK-decreasing K_{max} loading. For UHV, the T-L threshold value increases by ~0.7 MPa√m. The plateau transition from mechanically driven to hydrogen assisted crack growth for the 0.26 and 2.6 Pa environments is more apparent, and occurs at a slightly lower ΔK value than for the L-T orientation. Critically, Figure 4 shows a clear and novel threshold transition for water vapor pressures of 0.26 Pa and lower, similar to the L-T case. The da/dN minima occur at a ΔK of 4.5 to 4.3 MPa√m (R of 0.73 to 0.74) and a 5-fold reduction in P_{H2O} produces a 17-times decrease in

minimum da/dN. Absolute values of the da/dN minima are slightly lower for the T-L.[1]

The novel dependence of da/dN on ΔK and P_{H2O} for the L-T orientation of 7075-T651, measured under decreasing ΔK at a constant R of 0.5 (Figure 5), mirrors that for decreasing ΔK under constant K_{max} (Figure 3). For higher P_{H2O} above 4 Pa, da/dN depends on several power law segments of ΔK, consistent with literature expectations and HEE [7-9]. For UHV, single-slope Paris-law behavior transitions to Stage I and an apparent ΔK_{TH} of 5 MPa√m. Notably, the threshold transition response is observed for P_{H2O} levels between 0.02 Pa and 0.5 Pa (and perhaps as high as 1.8 Pa), where a 90-times reduction in P_{H2O} created a 9-times decrease in the minimum da/dN. The da/dN minima were observed for ΔK of 4.7 to 5.0 MPa√m at R of 0.50. These data establish that the threshold transition is not unique to a specific loading protocol or orientation. Furthermore similar behavior was observed in an Al-Li-Cu alloy [60].

Figure 6 plots data from Figure 5, as da/dN versus P_{H2O}/f for several constant ΔK levels at R of 0.5. The dashed trend lines in were drawn to both fit the specific data points and to comply with the following considerations: (a) environment independent FCP rate at UHV and low-rising P_{H2O}/f through 10^{-4} Pa-s, (b) Knudsen flow limited da/dN, directly proportional to P_{H2O}/f up to a saturation exposure, $P_{H2O\text{-}sat}$, of about 10^{-2} Pa-s, (c) a reduced dependence on exposure perhaps including possibility of an exposure independent da/dN plateau, and (d) a stronger exposure dependence. Compliance with these expectations is reasonable and systematic, but mechanistic justifications are somewhat controversial [17, 20, 21, 24, 25, 31]; these issues are considered in the Discussion.

---

1 While the novel growth rate dependence on ΔK is observed for each orientation, absolute values of da/dN exhibit modest differences between the L-T and T-L orientations. This difference may be due to different crack orientation in the partially recrystallized anisotropic microstructure, or to the different through-thickness location of the CT specimens (L-T at T/6 to T/7.3 and T-L at T/2 to T/3). Through-thickness hardness varied from R_B 93 at the surface to R_B 89 at T/2. Chemical composition varied from 2.46 wt% Mg, 1.57 wt% Cu, 5.65 wt% Zn at T/6 to 2.17 wt% Mg, 1.33 wt% Cu, 5.27 wt% Zn at T/2. Elemental segregation during ingot solidification typically enriches solute at the ingot surface compared to center and is somewhat retained during thermo-mechanical processing. The slower quench rate at plate center also results in a somewhat different precipitate distribution and size at T/2 compared to the surface. The governing factor(s) were not identified.

3.2 Fracture Surface Morphology

Each fatigue crack surface produced by decreasing ΔK loading was examined by low magnification optical microscopy. An example is shown in Figure 6b for an L-T specimen stressed at P_{H2O} of 0.5 Pa and constant R of 0.5. The fractograph shows a reflective, smooth surface (right) transitioning in the direction of crack growth to a rough surface (middle). This transition from smooth to rough fracture surfaces occurred for all decreasing ΔK experiments at P_{H2O} levels below 0.13 Pa (decreasing K_{max}) and 1.8 Pa (constant R), including UHV. This morphology change correlates with crack growth rate shifting from Paris Law to Stage I decreasing da/dN. This roughness changes suggests a microscopic mechanism transition with decreasing ΔK.

Two observations are notable for all specimens exhibiting the threshold transition behavior. First, the roughened region was coated with a black oxide that is presumably caused by fretting-contact of crack surface asperities in the presence of sufficient water vapor for oxidation (e.g., Figure 7b). Second, this roughened-black region transitioned back to a smooth-reflective surface with further increase in crack length (and decrease in ΔK). For example considering the L-T orientation and constant R loading, the smooth to rough and back to smooth crack surface morphology occurred for P_{H2O} levels of 1.8, 0.5, and 0.02 Pa where the threshold transition was observed. This correlation is quantitatively demonstrated in Figure 7 for P_{H2O} of 0.5 Pa. Vertical lines on the da/dN versus ΔK plot (Figure 7a) correspond to lines of matching style on the optical fractograph (Figure 7b) that denote the compliance indicated crack front location at each ΔK value. The region of the da/dN decline spans the crack length position of the black-roughened surface, which in this case formed an elliptically shaped front at the point of transition back to a smooth surface. Clearly, the near-threshold transition of da/dN through a minimum takes place concurrent with the increase in surface roughness, followed by a return to much less apparent roughness. The presence of such roughness, interacting with water vapor, likely plays a key role in the mechanism for this novel threshold transition, as developed in the Discussion.

The microscopic mechanism of FCP, and associated crack surface roughness, depends on ΔK and environment. SEM fractography of UHV K-shed fracture surfaces (Figure 8) for both T-L and L-T oriented specimens demonstrate faceted features (Figure 8a and 8c, respectively) at low ΔK. Prior work on this lot of material [61] and other precipitation hardened Al alloys [62, 63] cracked in inert environments used quantitative crack-surface stereology coupled with EBSD to

establish that such facets are characteristic of slip band cracking (SBC) parallel to {111} slip planes. Consistent with prior work, this SBC morphology is not observed at higher ΔK (Figure 8b and 8d), likely due to elimination of discretely localized planar slip banding through activation of multiple slip systems as the stress intensity range and crack tip plasticity increase. In this higher ΔK regime, the crack surface is flat, non-crystallographically based, and populated by a small fraction of void-like features, which suggest fatigue cracking about constituent particles [57]. Figure 9 shows the evolution of fatigue crack surface morphology at a fixed-low ΔK of 4.5 MPa√m (R = 0.5), with increasing water vapor pressure from 0.007 to 1,400 Pa for L-T specimens of 7075-T651 with corresponding growth rate data are reported in Figure 1. The SBC-like morphology in Figure 9a suggests crack growth governed by mechanical damage accumulation (i.e. no HEE contribution), consistent with a low exposure parameter (P_{H2O}/f = 3.3 x 10^{-4} Pa-s) and crack growth rates on the lower plateau in Figure 1. The density of faceted features attributed to SBC decreases with increasing P_{H2O}. Specifically, SBC-like features are sparsely observed at 0.06 Pa (Figure 9b), which is in the Knudsen flow regime (P_{H2O}/f = 3.3 x 10^{-3} Pa-s). The crack the morphology is fully transgranular, without SBC, at 6.6 Pa (Figure 9c; 0.3 Pa-s) and 1,400 Pa (Figure 9d; 70 Pa-s); both of which are in the saturation regime above P_{H2O}/f_{sat}, as developed in the Discussion. The two high exposure morphologies are consistent with prior results that showed H-enhanced fatigue propagation along {100}, {110}, or high index {hkl} planes, speculatively governed by hydrogen enhanced decohesion (HEDE) through cyclically developed dislocations structures [17, 35, 61-64]. These observations demonstrate that fracture surface morphology can be used to interpret the unique threshold transition behavior centered on HEE as the governing mechanism.

Figure 10 illustrates the morphology of the fatigue crack surface in the T-L orientation of 7075-T651 produced by decreasing ΔK-constant K_{max} loading at P_{H2O} equal to 0.13 Pa. The corresponding da/dN versus ΔK data are shown in Figure 3. The morphologies at ΔK above 5.4 MPa√m (Figures 10a through 10c) are similar to those produced by the UHV, 0.006, and 0.053 Pa environments; consistent with near identical growth rates. Such surfaces are flat, indicating slip on multiple systems at the crack front, typical of inert-benign environment morphologies in the mid-Paris regime. Crack features manifest small orientation changes at grain boundaries, indicating a weak effect of grain-to-grain crystallographic orientation variation on the microscopic crack path. Fatigue striations are observed; however, the average spacing is approximately ten

times the fatigue crack growth rate at these locations, indicating discontinuous crack advance. Consistent with the low-magnification optical image in Figure 7, the fracture surface morphology in the threshold transition regime (~4.5 MPa√m) shows a distinct change to anSBC-like morphology (Figure 10d). As the ΔK decreases to 3.3 MPa√m, out of the threshold transition regime, the crack surface morphology exhibits only sporadic SBC-like features (Figure 10e) as the da/dN increases. With further decrease in ΔK to 2.2 MPa√m, where the growth rate approaches that of higher exposures which do not exhibit the threshold transition, the crack morphology is fully transgranular with no indication of SBC-like features (Figure 10f).

With decreasing ΔK, the transition from SBC-like features and low growth rates at the da/dN minimum, to a transgranular morphology and higher growth rates, occurred for each specimen of 7075-T651 that exhibited the threshold transition. This conclusion is justified by the fractographic results in Figure 11 for a T-L oriented specimen at P_{H2O} of 0.053 Pa (ΔK of ~4.8 MPa√m in Figure 11a and 2.4 MPa√m in Figure 11b), with corresponding da/dN data shown in Figure 3. Figures 11c and 11d show a similar comparison for L-T orientated specimens at P_{H2O} of 0.5 Pa (ΔK of ~4.9 MPa√m in Figure 11c and 3.0 MPa√m in Figure 11d). Corresponding da/dN data and optical fractography are shown in Figure 7. In each comparison the higher ΔK level reasonably represents the minimum da/dN in the threshold transition, while the lower ΔK correlates with increased growth rates that have risen to levels typical of the higher exposure environments. The minimum da/dN crack surfaces show substantial roughness from SBC (Figures 11a and 11c), while the higher da/dN (lower ΔK) crack surfaces in Figures 11b, and 11d are microscopically flatter without resolvable SBC and typical of HEE associated with {100}, {110} and high index features. The more severe growth rate dips (corresponding to lower P_{H2O} values) exhibited a higher density of SBC-like features, thus higher roughness, as compared to less severe dips (higher P_{H2O} values). These trends were observed for each instance of the threshold transition, regardless of loading format or crack orientation. *In toto* the fractographic findings demonstrate that the onset of the threshold transition directly correlates with the appearance of a macroscopically rough crack surface, and the associated microscopic feature changes that suggest minimum HEE at the minimum da/dN in the threshold transition.

Discussion

The present experiments reveal both the expected strong-deleterious effect of water vapor on da/dN, governed by P_{H2O}/f (Figures 2 and 6), and a novel effect of water vapor on the ΔK dependence of da/dN in the near-threshold regime (Figures 3 through 5). For wide-range decreasing-ΔK loading, the FCP response of 7075-T651 in UHV is characterized by a single power law, transitioning to steeply declining da/dN with decreasing ΔK toward a ΔK_{th} of 3-5 MPa$\sqrt{m}$ (Figures 3 through 5). In contrast at higher water vapor pressures (> 0.25 Pa for constant K_{max} and > 4 Pa for constant R) da/dN declines through a series of power law segments for decreasing ΔK under both constant K_{max} and constant R-loading. No apparent threshold is observed for high R approaching 0.9 and ΔK as low as 1.5 MPa$\sqrt{m}$ for constant K_{max} data, whereas constant R of 0.5 data suggest a ΔK_{th} of 1.5 MPa$\sqrt{m}$ as da/dN falls below 10^{-7} mm/cyc, consistent with extensive results for this same lot of 7075-T651 stressed in moist air [55]. The water vapor environment resulted in a substantial reduction in threshold and increased da/dN at all ΔK levels. This behavior is well known and qualitatively understood based on hydrogen environment embrittlement interacting with crack closure [5-9, 55]. Growth rate degradation due to water vapor exposure is manifest by a change in the microscopic crack path, from slip band cracking to other transgranular damage mechanisms attributable to H embrittlement (Figures 8 and 10). As a result, the shift in threshold behavior due to water vapor is likely exacerbated by a strong effect of closure due SBC-based roughness unique to UHV, and transitioning to a less-rough crack morphology typical of HEE at P_{H2O} above 0.25.

A unique minimum in da/dN versus ΔK, the threshold transition regime, is reproducibly observed for two crack orientations of 7075-T651 (L-T in Figures 3 and 5, and T-L in Figure 4), as well as for two decreasing-ΔK loading protocols (constant K_{max} in Figures 3 and 4, and constant R in Figure 5). This behavior is observed in the lower growth rate regime (generally below 5×10^{-6} mm/cycle) and in a restricted water vapor pressure interval; specifically, 0.006 Pa to 0.25 Pa for constant K_{max} = 16.5 MPa$\sqrt{m}$ and 0.02 to 1.8 Pa for constant R = 0.5. In all cases the minimum value of da/dN falls systematically with decreasing P_{H2O}. Through this minimum, da/dN rises with further decreases in ΔK and approaches growth rates (about 10^{-6} mm/cycle) typical of higher water vapor pressures and very low ΔK. This unique growth rate response has here-to-fore not been reported for fatigue in precipitation hardened Al alloys because: (a) wide-ranging ΔK change

experiments have been limited to either inert UHV or high P_{H2O} environments, and (b) wide-ranging P_{H2O}/f change experiments have been limited to relatively high constant ΔK above about 6 MPa√m [5-9, 16, 17, 29, 37, 38, 40-42, 44-47, 49, 55, 65] As a single exception, Bradshaw and Wheeler reported da/dN versus increasing-applied ΔK trend lines (without supporting data) showing da/dN minima for an Al-Cu-Mg-Ni alloy stressed in 101 kPa N_2 or Ar plus water vapor with P_{H2O}/f from 0.4 Pa-s to 20.7 Pa-s [11, 66]. The minimum values of da/dN rose systematically from 3×10^{-6} to 8×10^{-5} mm/cyc as the exposure parameter increased over this range. The minima in da/dN were eliminated for water vapor at P_{H2O}/f of 20 Pa-s and 2000 Pa-s, without N_2 or Ar present. An explanation for this behavior was not presented [11].

The results in Figures 1 through 6, coupled with the fatigue crack surface features shown in Figures 7 through 11, provide a basis to consider two questions: (a) Is there a loading protocol-water vapor pressure interaction which impacts the magnitude and functional form of da/dN versus P_{H2O}/f, and (b) What is the mechanism for the occurrence of the minimum in da/dN? The latter question is particularly important given the potential for this behavior to introduce a false threshold-like response that could lead to erroneously-long fatigue lives from the standard fracture mechanics prediction approach [14].

4.1 Loading History Dependence

Figure 12 compares steady state fatigue crack growth rates in 7075-T651 measured under several loading protocols: (a) constant ΔK and constant R for a wide range of P_{H2O}/f (Figure 1), (b) continuously decreasing ΔK in these same environments for constant R (0.5, Figure 6), and (c) continuously decreasing ΔK for constant K_{max} of 16.5 MPa√m (R of 0.50 or 0.67 with ΔK of 8.3 or 5.5 MPa√m, respectively). The decreasing ΔK data points are limited to P_{H2O}/f and ΔK not outsidethe threshold transition regimes shown in Figure 2 and 4. Figure 12 shows that equal da/dN are produced at constant ΔK of 4.5 and 3.0 MPa√m (R = 0.50) for both constant ΔK (and ○) and continuously decreasing ΔK (■ and ●) formats at water vapor exposures above 0.01 Pa-s. The higher ΔK is just above the near threshold transition and the lower ΔK is well below this growth rate minima. Similarly, equal da/dN are produced at constant ΔK of 8.3 (R = 0.5) and 5.5 MPa√m (R = 0.66) for constant K_{max} loading (◆, ▲) compared to constant R (decreasing ΔK, ◆) and constant ΔK (Δ), respectively for a wide range of P_{H2O}/f where threshold transition behavior

does not occur. Fractography revealed flat transgranular features for all growth rates in Figure 12; the morphologies for high exposures at each ΔK mimicked Figures 9c and 9d, whereas the low exposures at ΔK of 5.5 MPa$\sqrt{m}$ resembled Figures 10a through 10c. These comparisons demonstrate that each loading protocol produces essentially identical P_{H2O}/f-dependent crack growth rate responses provided that: (1) the comparison is made at constant R, and (2) the exposure and/or ΔK is high enough to preclude increased crack wake roughness associated with SBC. These results affirm the original work by Wei and others, which focused on growth rates at ΔK levels well above the threshold transition regime and generally did not report drastic changes in fracture surface morphology [6, 19, 20, 23-27, 38, 41, 42].

Interacting effects of bulk P_{H2O}, crack wake roughness, ΔK and K_{max} on both crack closure and water vapor transport in the crack wake lead to deviations from the unique da/dN vs. P_{H2O}/f–relationships established in Figure 12. Figure 13 shows growth rate data from each loading protocol at a single ΔK of 4.5 MPa$\sqrt{m}$ and over a wide range of exposures. Growth rates for this L-T orientation differ for the same P_{H2O}/f depending on loading protocol. Higher da/dN at all exposures for decreasing ΔK-constant K_{max} loading (■) is consistent with 4.5 MPa$\sqrt{m}$ being above the threshold transition regime shown in Figure 2, and with flat-transgranular features observed for each constant K_{max} data point in Figure 13 (except UHV which demonstrated scattered SBC). The constant K_{max} growth rate data (■) illustrate the well-established effect of the higher R-value (0.73 for ■ versus 0.50 for ■ and) on closure and molecular flow. Qualitatively, the more open crack leads to a reduction in closure shielding, as well as a less impeded path for molecular flow and thus higher P_{H2O} at the crack tip; both factors enhance growth rates [38, 47].

However, even at a constant R, different loading protocols (histories) can result in crack wake fracture surface morphology changes that affect closure and water vapor transport to the crack tip. This is supported by three observations. First, a complicating influence of loading history is demonstrated in Figure 13 where for exposures less than 0.2 Pa-s, decreasing ΔK data (■) tend to be slower than constant ΔK rates ( ), despite identical-constant R of 0.5. The decreasing ΔK data which exhibit slower growth rates correspond to exposures (P_{H2O}/f of 0.09, 0.025, and 0.009 Pa-s) that experience the threshold transition in Figure 4 (P_{H2O} of 1.8, 0.5, and 0.18 Pa, respectively, at 20 Hz). For each exposure the onset of the threshold transition under decreasing ΔK begins at about 5.5 MPa$\sqrt{m}$ and is accompanied by transition to a rougher SBC

morphology; 1.8-2.5 mm of rough SBC crack extension occurs between 5.5 and 4.5 MPa√m (as illustrated in Figure 7 for P_{H2O}/f = 0.027 Pa-s). The constant ΔK data ( ) in Figure 13 resulted from two specimens where P_{H2O} was varied from low to high, with at most about 1.3 mm of SBC crack wake roughness prior to stressing in the exposure range of 0.0005 to 0.1 Pa-s. Lower da/dN for the decreasing ΔK case suggests that this greater crack wake area and more severe SBC roughness lead to a more potent reduction of da/dN, likely due to further impeded water vapor transport and enhanced closure.

A second indication of a stress intensity history effect on da/dN versus P_{H2O}/f is provided by the SEM image of a fatigue crack surface presented in Figure 14. The CT specimen was stressed at a single ΔK of 4.5 MPa√m (R = 0.5), with P_{H2O}/f changed from high (A) to very low (B, UHV) to high (C, >10 Pa-s). A similar result was observed for a specimen loaded at constant ΔK of 3.0 MPa√m (R = 0.5). Following the high P_{H2O}/f exposure (A), stressing in UHV caused a rough crack surface, represented by the reflective area (B) and likely associated with SBC of the sort shown in Figure 8. When the water vapor pressure was increased to exposure C, at the end of segment B, the crack grew inward from the CT specimen surfaces. Subsequent continued cycling in UHV created the crack shapes shown in regions D and E. The shape shown in Figure 14, and suggestion that crack growth proceeded along vectors starting at the corners noted by ●, is consistent with preferential water vapor diffusion, nominally parallel to the region B crack front and competing with impeded molecular transport in the direction normal to the region B crack front. The growth rates associated with regions A and B conformed with the results shown in Figure 1, but a slower rate was measured for segment C due to the crack shape change leading to inaccurate compliance and stress intensity solutions. This behavior was avoided if the da/dN segments were produced with progressively increasing P_{H2O} levels such that crack surface roughness decreased incrementally with modest increases in water vapor pressure (and da/dN), as implemented for the data in Figure 1.

A final indication of the importance of loading format and environmental exposure sequence is provided by the experiment represented in Figure 15. A T-L oriented CT specimen of 7075-T651 was cracked in UHV under constant K_{max}-decreasing ΔK to establish the ΔK_{TH} of about 4.2 MPa√m and compliance-indicated crack length of 30.64 mm (confirmed by optical measurement to equal 30.73 mm). Loading was suspended, water vapor (P_{H2O} = 0.26 Pa) was introduced, and (after a 7.5 h equilibration exposure without stress) cyclic loading was resumed at

20 Hz with ΔK programmed to decrease at the standard rate of the prior UHV experiment[2]. For the first 20 h of loading at 20 Hz, no crack extension was resolved by compliance change. Then da/dN progressively rose with decreasing ΔK, and increasing crack length, reaching a level equal to da/dN observed in Figure 3 for continuous decreasing of ΔK at constant P_{H2O} (0.26 Pa). The transient behavior in Figure 15 is consistent with the fact that initial cracking in UHV to near threshold produced a rough-faceted surface (see Figure 9). This rough crack wake impacted the molecular flow characteristics, which affected crack tip pressure, and may have affected a crack shape evolution in the manner show in Figure 14. Moreover, the rough UHV crack wake likely favored closure which retarded the initial 0.26 Pa growth rates below those observed in Figure 3. A flat transgranular morphology emerged as crack extension at 0.26 Pa continued with decreasing ΔK and da/dN approached the levels observed in Figure 3.

4.2 Mechanism for P_{H2O} and ΔK History Dependent da/dN

The crack growth rate results in Figure 12, plus fractographic findings in Figures 8 through 11, suggest a framework upon which to build mechanistic understanding of FCP growth rate response to wide-ranging stress intensity protocol interactions with water vapor exposure. For convenience, consider the schematic representation of da/dN versus normalized-effective ΔK shown in Figure 16 [37, 48].[3] The range of minimum values of da/dN in the threshold transitions regimes of 7075-T651 (Figures 3 through 5) is represented by the vertical bar. For high P_{H2O}/f at any ΔK, as well as at high ΔK for any water vapor exposure, da/dN declines primarily with decreasing ΔK and P_{H2O}/f, following the upper-two dotted lines in Figure 16. In these instances the crack wake is microscopically flat and neither da/dN minima nor loading protocol effects are observed. For loading in UHV and lower levels of P_{H2O}/f, the initial decrease in da/dN with decreasing ΔK into the threshold transition is exacerbated by increasing crack wake SBC roughness. This promotes closure and impeded water-molecule flow, thus decreasing the crack tip

---

[2] Upon reloading, the initial crack length was 30.93 mm, with the increase due to a compliance inaccuracy which caused the shift to slightly higher ΔK as shown in Figure 15.

[3] In this formulation, the environmental effect on da/dN is assumed to be due to either a water vapor adsorption impact on crack tip plasticity/surface energy or crack tip FPZ H embrittlement. For inert environments, Stage II intrinsic growth is governed by accumulation of Mode I crack tip opening strain, while Stage I growth is macroscopically Mode I but crystallographically oriented to create SBC facets on the microscopic scale [37, 48].

driving force and water vapor pressure at the crack tip, respectively. This is the classic transition from Stage II to Stage I FCP with decreasing ΔK, as illustrated by the transition between the two intrinsic lines in Figure 16. Continued decline in intrinsic Stage I da/dN is interrupted by a da/dN minimum, which begins the elimination of SBC and crack wake roughness. The proportion of microscopically flat crack surface, as well as da/dN, continuously rise with further decrease in ΔK to rejoin the much enhanced crack growth kinetics typical of higher levels of water vapor exposure and either of the water vapor adsorbate or hydrogen damage mechanisms [37, 48].

The total-measured da/dN for environment-sensitive fatigue cracking is given by the sum of three growth rate components [6]: (a) inert environment da/dN due to cyclic plasticity, independent of loading frequency, (b) time-cycle dependent da/dN_{cf} due to crack tip damage accumulation from interaction of cyclic plastic strain, tensile stress, H concentration, and/or a surface adsorbate/hard film effect on plasticity, and (c) "static load" environmental cracking at stress intensity levels in the load cycle which are above a threshold for monotonic load time-dependent cracking, da/dt, perhaps exacerbated by low amplitude cyclic loading. For lower ΔK levels, intrinsic plasticity (a) and time-cycle (b) contributions to da/dN are each likely discontinuous, requiring multiple cycles for a crack advance [7, 28]. The key mechanistic questions are: (1) how do the crack wake roughness, bulk and crack tip environment and decreasing ΔK interact to promote the Stage II to Stage I transition, and (2) what is the cause of the reversal from Stage I (inert environment) FCP, through the da/dN minimum and upward into the environment sensitive regime, as diagramed in Figure 16.

4.2.1 Static Load Cracking Mechanism

It is necessary to establish the extent to which the threshold transition behavior is explained by a change in the relative contributions of the static load environmental cracking component (c) and the ΔK-dependent time-cycle component, (b). At high ΔK in the Paris regime, (b) dominates the total da/dN owing to relatively slower da/dt. However, decreasing da/dN with decreasing ΔK could lead to an increased contribution of the static load da/dt component which scales with K_{max}. As such, the measured-total da/dN for a decreasing ΔK protocol would fall, then rise to a constant level for constant K_{max} testing (Figures 3-4) or to a mildly decreasing level for constant R testing (Figure 5). Essentially, the threshold transition could reasonably result from the

diminishing contribution of cyclic plastic strain, (b), leading to the decrease in growth rate followed by the onset of static load cracking, (c), to cause the subsequent increase in da/dN. This static load da/dN is approximated by the time dependent growth rate (da/dt) divided by loading frequency. As such, a da/dN of 1 x 10^{-6} mm/cycle (as observed in the post-minima region in Figures 3 through 5) is associated with da/dt of 2 x 10^{-5} mm/s at 20 Hz loading frequency. This level of static load cracking was reported as the upper bound possible for precipitation hardened Al alloys stressed at K levels above 5-12 MPa√m (depending largely on crack-grain orientation) in sufficiently aggressive-moist environments that produce crack tip H for HEE [67, 68].

Several factors suggest that the static-load cracking mechanism does not cause the da/dN minimum. First, the da/dN minimum is observed at the same ΔK of 4-5 MPa√m for constant K_{max} (of 16.5 MPa√m in Figures 3 and 4) and constant R (K_{max} of 8-10 MPa√m in Figure 5) experiments with the L-T and T-L orientations of 7075-T651. A similar transition at different K_{max}, and for different crack orientations, is not consistent with the static load mechanism. Second, a similar da/dt of 2 x 10^{-5} mm/s (associated with da/dN of 1 x 10^{-6} mm/cycle at 20 Hz in Figures 3, 4 and 5) is unlikely to be similarly produced by these two different K_{max} levels for these two different crack-grain orientation. Third, the low levels of P_{H2O} are likely insufficiently severe to produce the upper bound static load cracking rates (2 x 10^{-5} mm/s [67, 68]) necessary to explain the post-minima growth rates observed in Figures 3-5, where the K_{max} is as low as 4-8 MPa√m and the crack is not parallel to the rolling plane. Fourth, once da/dN rises from the minimum level, with decreasing ΔK at constant K_{max}, the results in Figures 3 and 4 show that da/dN merges with the declining growth rates typical of higher water vapor exposures. Critically, da/dN then falls with decreasing ΔK; this ΔK dependence is inconsistent with linear superposition of da/dt to create the da/dN minimum. Finally, severe static load cracking (resulting in growth rates of 2 x 10^{-5} mm/s) in peak-aged Al-Zn-Cu-Mg alloys typically exhibits an intergranular morphology; such morphology was not observed for any of the current specimens stressed in the threshold transition region.

4.2.2 Cycle-Time Dependent FCP Rate

The preceding discussion establishes that ΔK and P_{H2O}/f dependent behavior observed in Figures 3, 4 and 5 is not well described by a static-load cracking mechanism, suggesting that the

ΔK-dependent cycle-time component (b) governs the threshold transition behavior. In this paradigm, the effect of P_{H2O}/f on da/dN is described by three regions of growth rate limitation due to: (I) intrinsic-cyclic plasticity, due to insufficient water vapor at the crack tip to produce a meaningful amount of dissolved H in the crack tip FPZ [7, 37], (II) water vapor transport to the occluded crack tip [6, 20, 21, 23, 25-28, 37], and (III) H diffusion into the crack tip process zone [6, 17] or surface reaction rate limitation [20, 21, 27]. The threshold transition and stress intensity protocol effects are prevalent for the P_{H2O}/f and ΔK-K_{max} conditions where da/dN is limited by the transport of water molecules to the occluded crack tip. This conclusion is supported by the experimental results in Figure 6 for decreasing ΔK under constant R; the minima in da/dN occurred at ΔK of 5.5 to 4.5 MPa√m for experiments conducted at P_{H2O}/f values between 0.009 and 0.09 Pa-s. Similar support is provided by the data for decreasing ΔK at constant K_{max} (Figure 12 and 13).

4.2.2.1 Mechanisms of Molecular Transport

4.2.2.1.1 Knudsen Flow

The controlling mechanism for molecular transport to the crack tip is critical to properly modeling the dependence of Region II da/dN_{cf} on P_{H2O}. Wei and others propose that the P_{H2O} at the occluded crack tip is lower than the bulk P_{H2O} due to Knudsen flow impedance of water vapor molecules interacting with crack walls. Solving coupled differential equations that account for tip surface reaction and this impeded molecular flow yielded the prediction that da/dN_{cf} in Region II increases directly with P_{H2O}/f, as given by [6, 17, 19-21, 23-27]:

$$\left(\frac{da}{dN}\right)_{cf} = \frac{P_{H_2O}}{f}\left[436\frac{\beta}{\alpha N}f(R)\frac{\sigma_{ys}^{\ 2}}{kTE^2}\left(\frac{T}{M}\right)^{\frac{1}{2}}\right]\left(\frac{da}{dN}\right)_{cf-Sat} \qquad (1)$$

where f is frequency, N is the density of surface reaction sites (10^{19} Al atoms/m^2), k is the Boltzmann constant, T is absolute temperature, E is Young's modulus, M is the molecular weight of water vapor, f(R) is a function of stress ratio, and α and β are empirical constants related to crack surface roughness and flow geometry, respectively. The dashed lines in Figures 1, 6, 11 and 12 conform to a slope of 1.0 in Region II, for each ΔK and R level examined; experimental values

of total da/dN are reasonably consistent with this prediction (note that the inert environment component is assumed to be small so that total da/dN in these approximately equals da/dN_{cf} in Equation 1). Above a saturation exposure, $(P_{H2O}/f)_{sat}$, growth rates in Region III mildly increase with increasing P_{H2O}/f, likely rate limited by either crack-surface reaction site saturation, H diffusion in the crack tip FPZ, or a combination of these two factors [6, 17]. Equation 1 was derived to describe per-cycle crack advance over an increment of growth, which is proportional to the fractional-surface coverage of water vapor molecules and thus the surface concentration of H proportional to the extent of H_2O-Al reaction [20, 21]. This analysis was enhanced to include discontinuous cracking associated with an increment of growth per number of cycles necessary for damage accumulation; as is relevant to lower growth rates [28, 37, 48]. The direct proportionality between da/dN_{cf} and P_{H2O}/f (Equation 1) is not substantially altered for continuous versus discontinuous cracking.

With this foundation, we hypothesize that the onset of the threshold transition minimum in da/dN is caused by roughness induced changes in the mass transport behavior that alters the water vapor pressure at the fatigue crack tip. As ΔK decreases along the Stage II to I transition (Figure 16), crack growth rate is limited by Knudsen flow (Equation 1), which leads to reduced crack surface H_2O adsorbate and H reaction product coverage and thus to increasing proportion of intrinsic Stage I SBC. This crack wake roughness exacerbates the limitation of H_2O transport to the crack tip resulting in further P_{H2O} drop and accelerating decline of the environmental contribution, da/dN_{cf}. This behavior contributes to the steep ΔK dependence of da/dN in Stage I. Knudsen flow based modeling (Equation 1) captures this roughness induced retardation of molecular transport through changes in α and β. Fractographs Figures 7 and 8 provide evidence of this Stage II to Stage I transition as the threshold transition minimum is approached.

4.2.2.1.2 Laminar Flow (Advection)

The hypothesis above is developed in the context of the Knudsen flow model (Equation 1 and amplifications [28]) and is only strictly applicable if the molecular transport to the crack tip is governed by diffusion. Turnbull proposed an alternate transport mechanism, caused by crack surface cyclic displacement, including 2-dimensional flow in the crack growth direction and parallel to the crack front. This laminar flow mechanism is termed advection. The relative importance of each transport mechanism for a cracked specimen and loading condition was

considered for 1-dimensional flow in the direction of crack growth without mass transport parallel to the crack front [69-74]. Diffusion is increasingly less important and advection is enhanced due to increasing crack depth, decreasing average crack opening (governed by ΔK and K_{max}), and increasing f. Transport is diffusion limited for crack depths less than a critical distance (l_{crit}), while advection is dominant for deeper cracks. Turnbull estimated the l_{crit} where diffusion and advection are equivalently effective transport processes for an idealized smooth-surface trapezoidal crack of blunted tip opening displacement and elastic mouth opening displacement [71, 74]:

$$l_{crit} \approx (D_{H2O}/f)^{1/2} / (1 - R^{1/2}) \qquad (2)$$

where D_{H2O} is the diffusivity of water vapor molecules. The D_{H2O} for pure water vapor is 0.28 cm^2/s at 23°C and 100 kPa pressure [75].

D_{H2O} will increase with falling water vapor pressure proportionate to $1/P_{H2O}$ [76-78] but will decrease for restricted volumes with dimensions below the mean-free path of the molecules. Typical fatigue crack opening displacements are shown in Table 1 for CT specimen size and loading conditions typical of the threshold transition (e.g., Figure 7). The blunted-maximum crack tip opening displacement (CTOD) was given by $0.6K^2/2\sigma_{YS}E$ (from elastic-plastic analysis of the monotonic CTOD for a strain hardening alloy [79] and the superposition assumption that cyclic loading reduces the monotonic crack tip displacement by a factor of 2 [5, 9]). The elastic crack opening displacement (COD) was estimated as a function of position along the crack wake using a beam deflection model with linear displacement between 0 at the crack tip and the compliance-based value at the CT specimen edge. Each of these crack opening lengths is orders of magnitude smaller than the mean-free path for water molecules (4.2 cm at P_{H2O} of 0.25 Pa based on the kinetic theory of an ideal-pure gas [77]). As such, water molecule collisions with the occluded crack wall (Knudsen flow) reduce D_{H2O} well below the level typical of bulk flow, particularly at low P_{H2O}, and thus hinder diffusional transport of water to the reacting tip. The D_{H2O}, modified for Knudsen flow in an idealized-cylindrical channel of radius equaling half of the average COD (0.7 μm from Table 1), is 3 cm^2/s and therefore the l_{crit} (Equation 2) is 1.3 mm. This critical distance is equal or smaller than the crack depth ahead of the CT specimen notch root (about 1.3 cm at the onset of the da/dN minima in Figures 3 through 5) and the specimen half-thickness (3.2 mm).

The simplicity of this idealized 1-D cylindrical channel analysis (Equation 2) prohibits a definitive determination of the relative influence of diffusion and advection; however the results inform the following considerations. First, advection feasibly contributes to the supply of crack tip water vapor. Second, further study is necessary to establish the critical distance for 2-D flow conditions and to quantify the effect of roughness and frequency on the advection mechanism. Third, a role of advection reduces the strict relevance of Equation 1 and suggests deviations from the da/dN $\approx P_{H2O}/f$ relationship in the transport controlled regime. Fourth, a contribution of advection does not compromise the hypothesis that roughness induced impeded flow (either diffusion or advection controlled) exacerbates the transition from Stage II to Stage I cracking at low P_{H2O}/f. While a potential contribution of advection is recognized, for simplicity further discussion assumes a diffusion (Knudsen flow) controlled mechanism.

Table 1. Fatigue crack opening displacements relevant to the threshold transition shown in Figure 7.

	Blunted CTOD μm	COD at 0.5 mm μm	COD at 3.0 mm μm
Maximum	2.4	2.5	6.3
Minimum	0.7	0.6	2.7
Range	1.7	1.9	3.6
Average	1.5	1.6	1.6

Compact tension specimen, K_{max} = 16.5 MPa√m, crack length a = 21 to 22 mm, K gradient governed by C = -0.07 mm^{-1}

4.2.2.2 Threshold Transition Behavior

The onset of the apparent threshold intermediate P_{H2O}/f for decreasing ΔK loading protocols is due to the increase in crack surface roughness with decreasing ΔK due to increasing proportion of microscopically faceted SBC. Molecular flow to the crack tip is impeded, crack tip water vapor pressure declines and da/dN continues to fall more strongly dictated by β/α in Equation 1 for Knudsen flow controlled conditions. The additional contribution of low momentum lamellar advection at low-local P_{H2O} is also impacted by the irregular flow channel that develops along the microscopically rough crack wake. This self-perpetuating cycle further starves the crack tip of P_{H2O} and contributes to the steep ΔK dependence of da/dN at the onset of

the threshold transition behavior and increasing proportion/magnitude of SBC-based roughness. How the governing molecular flow mechanism changes with increasing crack depth and varying crack wake morphology is critical to interpreting the threshold transition behavior.

Increasing crack depth and decreasing average crack opening (governed by ΔK and K_{max}) will increase the relative contribution of lamellar water vapor flow by advection compared diffusion; however such changes are likely insufficient to explain why P_{H2O} rises with decreasing ΔK (at constant R or constant K_{max}) to create the da/dN minimum. Figure 17 shows that changes in crack opening displacement, with increasing crack length over the range typical of a threshold transition (e.g., 21 to 23 mm for the case illustrated in Figure 7), are not sufficient to dramatically impact water vapor transport to the crack tip. For example, the COD averaged over a load cycle is constant at the 3.0 mm location (4.8 μm) and increases by only 7% at the 0.5 mm location (14.5 to 15.5 μm) as crack growth continues through the da/dN minimum. This small increase in average opening compared to the large mean-free-path of water molecules (about 4.2 cm), and small decrease (10%) in cyclic COD over a small decrease in ΔK at constant f, should not impact the supply of water vapor. Some other factor must govern water vapor transport, sensitive to stress intensity level and protocol.

We propose that when either a critical span and/or magnitude of roughness is achieved the water vapor transport mechanism changes Knudsen flow and/or advection to fully turbulent convective mixing due to crack surface asperity contact on the microscopic scale and high frequency loading (e.g., 20 Hz). Such local contact imparts high momentum to injecting and exhausting molecules, as well as creating local turbulence and disorderly flow [69, 70, 73]. In the limit this transport enhancement enables the crack tip water vapor pressure to reach the bulk P_{H2O}, which was not possible due to either Knudsen flow diffusion or lamellar advection. This increased P_{H2O} feeds increased crack tip embrittlement and increasing da/dN_{cf}. Initially, such transport would be marginally enhanced as cracking continues to be rough and tortuous until sufficient P_{H2O} is delivered to crack tip to support the environmental contribution and return of microscopically flat crack surface features. With continued cyclic and declining ΔK, the proportion of SBC declines and is replaced by flatter {110}/{100}/substructure cracking [35, 62]. The da/dN approaches the level characteristic of decreasing ΔK loading in the higher P_{H2O}/f cases, which never developed the rough zone-impedance of Knudsen flow. The minimum level of da/dN

from Figures 3 and 4 is proportional to P_{H2O}/f raised to a power of 1.5 (L-T, Figure 3) to 1.8 (T-L, Figure 4). It is reasonable to expect that the magnitude of the drop and enhancement in crack tip water vapor pressure, thus da/dN, depend on bulk P_{H2O}. Lower bulk pressure means a rougher Stage I crack wake, as well as lower crack tip pressure delivered by turbulent convection leading to a slower recovery of da/dN with increasing crack length.

Microscopic crack surface roughness in the threshold transition (e.g., Figures 7, 8a and 9a) is sized on the order of the various crack opening displacements noted in Table I and Figure 17. The {111} facet height developed during SBC is on the order of half of the grain size measured in the S direction, suggesting that SBC peak-to-valley roughness is in the range of 5 to 20 μm for L-T and 5 to 35 μm for T-L oriented CT specimens. Crack opening varied during a load cycle at constant K_{max} (Table 1 and Figure 17) from 0.6 μm (at K_{min}) to 2.4 μm (at K_{max}) at the blunted tip, and from 2.7 μm to 6.3 μm at 3 mm behind the tip, each during a load cycle. These estimates support the notion of asperity contact, which is particularly favored by mixed mode SBC. The oxidized band on the fatigue crack surface, spanning the crack length interval over which the da/dN minimum occurs (Figure 7), supports fretting due to asperity contact, which interacted with the finite amount of water vapor presented to the reactive Al surface. Precise quantitative roughness measurements in the threshold transition zone are needed.

The effect of complex crack wake geometry and surface contact on the transition from orderly lamellar advection to turbulent flow to/from the crack tip has not been modeled to verify the proposed hypothesis. However, the hypothesis that a threshold level of roughness is needed to initiate asperity contact and turbulent flow is consistent with the work of Somerday and coworkers. They argued that for a flat crack wake morphology (no rough-faceted Stage I FCP) advection is lamellar for H_2 flow in a fatigue crack in steel; specifically, flow is dominated by the low dynamic viscosity of a gas (particularly at low pressures) and associated-low Reynolds number [80]. However, these workers acknowledged the possibility of turbulence due to crack wake asperity contact leading to equilibration of the crack tip gas pressure with that of the bulk environment.

In the context of the turbulent mixing hypothesis, two questions require additional discussion: (1) Why does da/dN rise from the minimum over a prolonged amount of crack growth and cyclic-loading time, and (2) Why does da/dN persist at levels consistent with cracking

at higher P_{H2O} after substantial crack growth? Figures 3 through 5 and 7 show that the rate of environmental fatigue crack propagation monotonically rises from the da/dN minimum with decreasing ΔK and over several milli-meters of crack growth. This behavior is not consistent with the onset of turbulent mixing across the entire crack front which would imply an abrupt rise in crack tip P_{H2O} leading to an abrupt rise in da/dN; this discrepancy is rationalized in two ways. First, turbulent mixing is likely to preferentially provide water vapor to the crack tip adjacent to boldly exposed surfaces, rather than uniformly along the Stage I crack front, creating an initial-irregular crack as evidenced by the environment change experiment represented in Figure 14. Fracture surface morphology in the post-minima region for data in Figure 3 through 5 indicate a similar complex crack front where environment enhanced transgranular fracture dominates at surface and SBC persists in the high-constraint center of the specimen; detailed analysis of this crack front evolution is ongoing. Second, through the da/dN minimum, and above, remnant SBC-wake roughness could create a tortuous flow channel that would both block full-convective mixing with the surrounding environment and favor crack closure to reduce the effective ΔK. This suggestion is supported by the UHV to water vapor (P_{H2O} of 0.26 Pa) change experiment represented in Figure 15; nil crack growth during the first 20 h of loading at 20 Hz was followed by a steady rise in measured da/dN. Each of these factors would initially retard da/dN, but be progressively reduced in importance as regions of rough SBC transitioned to the flatter-transgranular environmental cracking morphology.

Considering the second question, once the flat morphology and higher growth rates developed, the crack wake roughness progressively moved behind the crack tip. At some point, the rough zone should be sufficiently behind the crack tip so that asperity contact and local turbulent mixing no longer influence crack tip water vapor supply. The dominant molecular transport method would revert back to Knudsen flow or advection (parallel to the crack front) leading to a decrease in crack tip water vapor pressure and a decline in da/dN similar to that observed at the onset of the threshold transition regime for low P_{H2O}/f. Rather, da/dN measured for decreasing ΔK after the growth rate minimum, rises to approach the higher P_{H2O}/f growth rates over a crack advance distance of 3 to 6 mm. A sharp decline to crack arrest was not observed for constant K_{max} testing as shown in Figures 3 and 4; specifically, da/dN after a minimum does not evidence a Stage I-like decline for ΔK as low as 2 MPa$\sqrt{m}$ (R = 0.88) at P_{H2O}/f of 2.7×10^{-3} Pa-s. The estimated peak-to-valley roughness of the post-minima crack wake, formed by the presence of

water vapor, is on order of 1-3 μm which is well below the 5 μm to 35 μm typical of SBC. For the constant K_{max} data reported in Figure 3, the minima at 4 MPa√m occurs at a crack length of 31 mm and subsequent environmentally assisted transgranular cracking continues through 2 MPa√m at 41 mm. Figure 17 shows the change in various crack opening displacements associated with crack length increase from 31 mm to 41 mm. The maximum COD at 0.5 mm behind the crack tip (2.5 μm) is constant with this crack growth, and actually slightly decreases (from 5.6 μm to 5.5 μm) at the 3.0 mm location. The minimum COD at the 0.5 mm and 3.0 mm locations rises as the crack grows from 31 mm (1.5 μm or 3.7 μm, respectively) to 41 mm (1.9 μm to 4.5 μm, respectively) consistent with increasing R to very high levels at constant K_{max}. For this crack length change, the per-cycle average crack opening only modestly changes from 1.9 μm to 2.1 μm for the 0.5 mm location and 4.8 μm to 5.0 μm for the 3.0 mm location. It appears that continued turbulent mixing is provided by roughness from SBC located 5 to 10 mm behind the grown crack tip, or the residual microscopic roughness typical of environmental cracking is sufficient to create asperity contact nearer to the crack tip owing to the relatively low values of minimum COD. This environmental contribution could be magnified by the very high K_{max} typical of the constant K_{max}-decreasing ΔK protocol. The results in Figure 5 show that da/dN for all P_{H2O}/f appear to decline at an increasing rate at very low ΔK levels (below about2 MPa√m) for constant R of 0.5. This result suggests that intrinsic Stage I behavior will be recovered at sufficient low ΔK where both the crack tip water vapor pressure and closure-sensitive mechanical driving force are sufficiently reduced to eliminate the environmental contribution.

4.2.3 Mechanism of Environmental Damage

The preponderance of evidence and modeling supports crack tip fracture process zone hydrogen embrittlement as the dominant mechanism for the environmental contribution to fatigue crack propagation in Al alloys [5-9, 34, 35, 37, 39, 41, 48]. The prior discussion has rationalized the threshold transition behavior in terms of this hydrogen embrittlement mechanism. However, alternate hypotheses attribute da/dN enhancement to: (a) a crack tip surface film ($Al_x(OH)_y$ and Al_2O_3 from water vapor or O_2 reaction) on process zone dislocation structure evolution [11, 36, 66], (b) absorbate (H_2O)-reduced surface energy and enhanced dislocation emission [7, 8, 33, 34,

37, 48, 81], or (c) elimination of asperity welding [11, 40]. The threshold transition behavior is considered in the context of these alternate hypotheses.

The water molecule adsorption and hard-surface film mechanisms do not appear to explain the da/dN minima observed in the present work. Petit and coworkers advocate that da/dN_{cf} is composed of the linear superposition of a H-assisted damage term plus a contribution from water-adsorbate reduction of surface energy leading to enhanced crack tip opening/plasticity and reduced critical displacement/energy for crack growth [7, 8, 37, 48, 81]. From Figure 16, H-enhancement dominates da/dN at total growth rates below 1-2 x 10^{-5} mm/cycle [28, 37, 48]. The interesting threshold transition region in the present study occurs at growth rates well below this level, supporting the H embrittlement framework. Furthermore, testing of peak aged Al-Li-Cu alloy stressed over a wide range of ΔK in high purity O_2, N_2, Ar and ultra-high vacuum (~0.25 μPa residual pressure) [39] produced identical da/dN, suggesting that a hard-surface film does not impact crack tip plasticity damage. However, a film-based mechanism may have been responsible for a mild deleterious effect of pure O_2 (ultra-high vacuum conditions where used to minimize H_20 contamination) on FCP in Al-Zn-Mg-Cu [11, 39, 66]. While O_2 contamination was not a factor in the present experiments a similar film effect from H_2O-Al reaction may have played a second-order role in da/dN enhancement for 7075-T651 stressed in the low growth rate regime. Such a film could impact both crack tip plasticity [36, 39, 66], as well as the extent of water vapor surface reaction and H uptake [82].

Chawla and coworkers demonstrated strong-transient effects of changing ΔK and K_{max} loading protocol on da/dN for the UHV environment, interpreted as caused by asperity welding [40]. However, this study did not evidence a da/dN minimum for any loading or environmental condition. In principle as ΔK and da/dN declined in the Stage I region for UHV and low P_{H2O}/f environments, $Al_x(OH)_y$ from water vapor reaction with Al would be hindered by highly impeded water molecule transport. Crack tip plasticity accumulation and asperity welding (potentially due to the lack of oxide formation [40]) would be unhindered and da/dN would fall precipitously in a classic Stage I response. Upon introduction of water vapor by the turbulent-convection mechanism, Al oxidation by water could lead to a surface film, which reduces local welding [40] and/or favors damage from altered dislocation structure [36, 66]. The fatigue crack growth rate could, under these circumstances, rise with falling da/dN, paralleling the hypothesized increase in

da/dN_{cf} due to H embrittlement. These alternate damage-mechanism possibilities do not alter the primary explanation that the da/dN minimum is due to a transition in the water vapor transport mechanism.

Conclusions

Based on the work performed in this study, the following conclusions are established for water vapor sensitive fatigue crack propagation in a peak-aged Al-Zn-Mg-Cu alloy.

1) Fatigue crack growth rate (da/dN) in 7075-T651 aluminum plate decreases with decreasing water vapor pressure over a very wide range of stress intensity range (ΔK) and maximum stress intensity (K_{max}) levels.

2) The water vapor pressure dependence of da/dN is understood based on the established processes of Knudsen diffusion of water vapor molecules to the occluded crack tip, surface reaction to produce atomic H, H diffusion into the crack tip fracture process zone, and H-plasticity-stress interaction.

3) A novel minimum in da/dN is observed for low ΔK and an intermediate range of water vapor pressures; where the initial decline in Stage I growth, toward the UHV threshold transitions to increasing da/dN with further decreases in ΔK and which merges at very low ΔK with growth rates typical of higher water vapor pressures. This behavior is observed during decreasing ΔK at both constant K_{max} and constant R.

4) The fatigue cracking mode changes from flat-transgranular (Stage II) to crystallographic slip band cracking (Stage I) with decreasing fatigue crack growth rates into the threshold region for inert-benign environments. Cracking in higher pressure water vapor is flat and transgranular for all stress intensity conditions examined, consistent with hydrogen environment embrittlement. For intermediate water vapor pressures, the da/dN minimum correlates with a transition from roughened-oxidized slip band facets to the smooth morphology characteristic of high water vapor pressures.

5) The da/dN minimum is explained based on increased water vapor supply to the crack tip due to the onset of turbulent-convective mixing form Stage I crack surface, thus reigniting hydrogen environment embrittlement which would otherwise not occur at low water vapor pressures governed by Knudsen diffusion and orderly lamellar advection.

6) The da/dN minima occur for a wide range of stress ratio loading conditions, for applied ΔK of 4-5 MPa$\sqrt{m}$. Low rates of Stage I fatigue cracking, which precede the onset of the da/dN minimum can lead to a false-high threshold stress intensity range for low water vapor pressure environments.

Acknowledgements

This research was sponsored by the Total Corrosion Collaboration managed by the DoD Office of Corrosion Policy and Oversight. Drs. John Papazian (deceased) and Elias Anagnostou of Northrop Grumman Corporation provided 7075-T651, as well as Northrop Grumman Industry Liaison funding. These contributions are gratefully acknowledged. The views and conclusions contained herein are those of the authors and should not be interpreted as necessarily representing the official polices and endorsements, either expressed or implied of US Air Force Academy or the US Government.

References:

[1] P.C. Paris, F. Erdogan, J. Basic. Engr. Trans. ASME, Series D, 86 (1963) 528-534.

[2] A.K. Vasudevan, K. Sadananda, N. Louat, 2 Critical Stress Intensities for Threshold Fatigue Crack-Propagation, Scripta Metallurgica Et Materialia, 28 (1993) 65-70.

[3] S. Dinda, D. Kujawski, Correlation and prediction of fatigue crack growth for different R-ratios using K-max and Delta K+ parameters, Eng Fract Mech, 71 (2004) 1779-1790.

[4] A.K. Vasudevan, K. Sadananda, A viewpoint on environmental contributions to fatigue crack growth, Int J Mater Prod Tec, 30 (2007) 3-16.

[5] R.P. Gangloff, M.B. Ives, Environment-Induced Cracking of Metals; NACE-10, in, NACE International, Houstone, TX, 1990.

[6] R.P. Wei, Fracture Mechanics : Integration of Mechanics, Materials Science, and Chemistry, Cambridge University Press, Cambridge England ; New York, 2010.

[7] J. Petit, G. Henaff, C. Sarrazin-Baudoux, Environmentally asisted fatigue in the gaseous atmosphere, in: J. Petit, P. Scott (Eds.) Comprehensive Structural Integrity: Environmentally Assisted Fracture, Elsevier, New York, NY, 2003, pp. 962-970.

[8] J. Petit, J.D. Fouquet, G. Henaff, in: A. Carpinteri (Ed.) Handbook of Fatigue Crack Propagtion in Metallic Structures, Elsevier Science, Amsterdam, Netherlands, 1994, pp. 1159-1203.

[9] R.P. Gangloff, Environment sensitive fatigue crack tip processes and propagation in aerospace aluminum alloys, in: A. Blom (Ed.) Fatigue 2002, EMAS, Stockholm, Sweden, 2002.

[10] R.J.H. Wanhill, Corrosion Fatigue of Aircraft Materials, in, North Atlantic Treaty Organization, Neuilly Sir Seine, France, 1977, pp. 2-1 to 2-37.

[11] F.J. Bradshaw, C. Wheeler, International Journal of Fracture Mechanics, 5 (1969) 255-262.

[12] A.K. Vasudevan, K. Sadananda, G. Glinka, D. Kujawski, System and Method for Predicting Material Fatigue and Damage, in, 2011.

[13] J.E. Bozek, J.D. Hochhalter, M.G. Veilleux, M. Liu, G. Heber, S.D. Sintay, A.D. Rollett, D.J. Littlewood, A.M. Maniatty, H. Weiland, R.J. Christ, J. Payne, G. Welsh, D.G. Harlow, P.A. Wawrzynek, A.R. Ingraffea, A geometric approach to modeling microstructurally small fatigue crack formation: I. Probabilistic simulation of constituent particle cracking in AA 7075-T651, Model Simul Mater Sc, 16 (2008) 1-28.

[14] Online Damage Tolerant Handbook: www.afgrow.net/applications/DTDHandbook/. in, US Air Force Research Lab.

[15] G.H. Bray, R.J. Bucci, R.L. Brazil, Mat Sci Forum, 331-337 (2000) 1143-1156.

[16] D. Li, R.P. Gangloff, G.H. Bray, M. Glazov, R.J. Rioja, Ageing dependent intrinsic fatigue crack propagation in AA2024, in: M. Tiryakioglu (Ed.) Advances in the Metallurgy of Aluminum Alloys, ASM International, Materials Park, OH, 2001, pp. 105-118.

[17] Y.J. Ro, S.R. Agnew, G.H. Bray, R.P. Gangloff, Environment-exposure-dependent fatigue crack growth kinetics for Al-Cu-Mg/Li, Materials Science and Engineering A, 468 (2007) 88-97.

[18] J.T. Burns, R.P. Gangloff, Scientific advances enabling next generation management of corrosion induced fatigue, Procedia Engineering, 10 (2011) 362-369.

[19] R.P. Wei, R.P. Gangloff, in: R.P. Wei, R.P. Gangloff (Eds.) Fractuer Mechanics: Perspective and Directions, ASTM STP 1020, ASTM International, West Conshohocken, PA, 1989, pp. 233-264.

[20] T.W. Weir, G.W. Simmons, R.G. Hart, R.P. Wei, Model for surface-reaction and transport controlled fatigue crack-growth, Scripta Metall Mater, 14 (1980) 357-364.

[21] R.P. Wei, P.S. Pao, R.G. Hart, T.W. Weir, G.W. Simmons, Fracture-mechanics and surface-chemistry studies of fatigue crack-growth in an aluminum-alloy, Metall Trans A, 11 (1980) 151-158.

[22] M.R. Achter, Scripta Metall Mater, 2 (1968) 525-528.

[23] R.P. Wei, Environmental considerations for fatigue cracking, Fatigue Fract Eng M, 25 (2002) 845-854.

[24] M. Gao, P.S. Pao, R.P. Wei, Chemical and metallurgical aspects of environmentally assisted fatigue crack-growth in 7075-T651 aluminum-alloy, Metall Trans A, 19 (1988) 1739-1750.
[25] P.S. Pao, M. Gao, R.P. Wei, Critical assessment of the model for transport-controlled fatigue crack growth, in: R.P. Wei, R.P. Gangloff (Eds.) Basic Questions in Fatigue, ASTM STP 924, ASTM International, West Conshohocken, PA, 1988, pp. 182-195.
[26] P.S. Pao, M.N. Gao, R.P. Wei, Environmentally Assisted Fatigue-Crack Growth in 7075 and 7050 Aluminum-Alloys, Scripta Metall Mater, 19 (1985) 265-270.
[27] R.P. Wei, M. Gao, P.S. Pao, Scripta Metall Mater, 18 (1984) 1195-1198.
[28] G. Henaff, K. Marchal, J. Petit, On Fatigue-Crack Propagation Enhancement by a Gaseous Atmosphere - Experimental and Theoretical Aspects, Acta Metall Mater, 43 (1995) 2931-2942.
[29] J. Ruiz, M. Elices, Effect of water vapour pressure and frequency on fatigue behaviour in 7017-T651 aluminium alloy plate, Acta Mater, 45 (1997) 281-293.
[30] N.J.H. Holroyd, D. Hardie, Factors controlling crack velocity in 7000 series aluminum-alloys during fatigue in an aggressive environment, Corros Sci, 23 (1983) 527-&.
[31] Z.M. Gasem, R.P. Gangloff, Rate-limiting processes in environmental fatigue crack propagation in 7000-series aluminum alloys., in: R.H. Jones (Ed.) Chemistry and electrochemistry of corrosion and stress corrosion cracking: A symposium honoring the contributions of R.W. Staehle, TMS-AIME, Warrendale, PA, 2001, pp. 501-521.
[32] A.D.B. Gingell, J.E. King, The effect of frequency and microstructure on corrosion fatigue crack propagation in high strength aluminium alloys, Acta Mater, 45 (1997) 3855-3870.
[33] S. Lynch, Hydrogen embrittlement phenomena and mechanisms, Corros Rev, 30 (2012) 105-123.
[34] S. Lynch, in: R.P. Gangloff, B.P. Somerday (Eds.) Gaseous Hydrogen Embrittlement of Materials In Energy Technologies, Vol. 1, Woodhead Publishing Limitted, Cambridge, UK, 2012, pp. 274-346.
[35] Y. Ro, S.R. Agnew, R.P. Gangloff, Effect of Environment on Fatigue Crack Wake Dislocation Structure in Al-Cu-Mg, Metall Mater Trans A, 43A (2012) 2275-2292.
[36] M.J. Hordon, Acta Metallurgica, 14 (1966) 1173-1178.
[37] J. Petit, C. Sarrazin-Baudoux, Some critical aspects of low rate fatigue crack propagation in metallic materials, Int J Fatigue, 32 (2010) 962-970.
[38] J. Ruiz, M. Elices, The role of environmental exposure in the fatigue behaviour of an aluminium alloy, Corros Sci, 39 (1997) 2117-2141.
[39] R.S. Piascik, R.P. Gangloff, Environmental fatigue of an Al-Li-Cu alloy 1. Intrinsic crack-propagation kinetics in hydrogenous environments, Metall Trans A, 22 (1991) 2415-2428.
[40] A. Bonakdar, F. Wang, J.J. Williams, N. Chawla, Environmental Effects on Fatigue Crack Growth in 7075 Aluminum Alloy, Metall Mater Trans A, 43A (2012) 2799-2809.
[41] J. Ruiz, M. Elices, Environmental fatigue in a 7000 series aluminium alloy, Corros Sci, 38 (1996) 1815-1837.
[42] D.L. Dicus, in: S.W. Dean, E.N. Pugh, G.M. Ugiansky (Eds.) Evneironment-Sensitive Fracture: Evaluation and Comparison of Test Methods, ASTM STP 821, ASTM International, West Conshohocken, PA, 1984, pp. 513-533.
[43] H.J. Gudladt, J. Petit, Stage-Ii Crack-Propagation of Al-Zn-Mg-Single Crystals in Dry and Wet Atmospheres, Scripta Metallurgica Et Materialia, 25 (1991) 2507-2512.
[44] B. Holper, H. Mayer, A.K. Vasudevan, S.E. Stanzl-Tschegg, Near threshold fatigue crack growth at positive load ratio in aluminium alloys at low and ultrasonic frequency: influences of strain rate, slip behaviour and air humidity, Int J Fatigue, 26 (2004) 27-38.
[45] D.C. Slavik, C.P. Blankenship, E.A. Starke, R.P. Gangloff, Intrinsic fatigue-crack growth-rates for Al-Li-Cu-Mg alloys in vacuum, Metall Trans A, 24 (1993) 1807-1817.
[46] R.D. Carter, E.W. Lee, E.A. Starke, C.J. Beevers, The Effect of Microstructure and Environment on Fatigue Crack Closure of 7475-Aluminum Alloy, Metall Trans A, 15 (1984) 555-563.

[47] T.H. Shih, R.P. Wei, The Effects of Load Ratio on Environmentally Assisted Fatigue Crack-Growth, Eng Fract Mech, 18 (1983) 827-837.
[48] S. Richard, C. Gasqueres, C. Sarrazin-Baudoux, J. Petit, Coupled influence of microstructure and atmosphere environment on fatigue crack path in new generation Al alloys, Eng. Fract. Mech., 77 (2010) 1941-1952.
[49] G.H. Bray, M. Glazov, R.J. Rioja, D. Li, R.P. Gangloff, Int J Fatigue, 23 (2002) S265-S276.
[50] W.A. Herman, R.W. Hertzberg, R. Jaccard, A simplified laboratory approach for the prediction of short crack behavior in engineering structures, Fatigue Fract Eng M, 11 (1988) 303-320.
[51] J. Papazian, E.L. Anagnostou, R.J. Christ, S.J. Engel, D. Fridline, D. Hoitsma, J. Madsen, J. Nardiello, J. Payne, R.P. Silberstein, G. Welsh, J.B. Whiteside, DARPA/NCG structural integrity prognosis system, HR0011-04-C-0003, in, DARPA, Arlington, VA, 2009.
[52] J.M. Papazian, E.L. Anagnostou, S.J. Engel, D. Hoitsma, J. Madsen, R.P. Silberstein, G. Welsh, J.B. Whiteside, A structural integrity prognosis system, Eng Fract Mech, 76 (2009) 620-632.
[53] J. Payne, G. Welsh, R.J. Christ Jr, J. Nardiello, J.M. Papazian, Observations of fatigue crack initiation in 7075-T651, Int J Fatigue, 32 (2010) 247-255.
[54] A.D. Rollett, R. Campman, D. Saylor, in: Proceedings of 10th International Conference on Aluminum Alloys, 2006, pp. 1-10.
[55] J.C. Newman, E.L. Anagnostou, D.T. Rusk, Int J Fatigue, 62 (2014) 133-143.
[56] ASTM, E647-05: Standard test methods for measurement of fatigue crack growth rates, Vol. 03.01., in, ASTM International, West Conshohocken, PA, 2006.
[57] R. Sunder, W.J. Porter, N.E. Ashbaugh, Fatigue voids and their significance, Fatigue Fract Eng M, 25 (2002) 1015-1024.
[58] S.C. Forth, J.C. Newman, R.G. Forman, On generating fatigue crack growth thresholds, Int J Fatigue, 25 (2003) 9-15.
[59] J. Newman, J. Schneider, A. Daniel, D. McKnight, Compression pre-cracking to generate near threshold fatigue-crack-growth rates in two aluminum alloys, Int J Fatigue, 27 (2005) 1432-1440.
[60] J.T. Burns, Effect of water vapor pressure on the fatigue crack propagation of aerospace aluminum alloys 7075-T651 and 2199-T86, Proceedings of DoD Corrosion Conference, (2013).
[61] V.K. Gupta, S.R. Agnew, Fatigue crack surface crystallography near crack initiating particle clusters in precipitation hardened legacy and modern Al-Zn-Mg-Cu alloys, Int J Fatigue, 33 (2011) 1159-1174.
[62] Y. Ro, S.R. Agnew, R.P. Gangloff, Environmental fatigue-crack surface crystallography for Al-Zn-Cu-Mg-Mn/Zr, Metall Mater Trans A, 39A (2008) 1449-1465.
[63] Y. Ro, S.R. Agnew, R.P. Gangloff, Crystallography of fatigue crack propagation in precipitation-hardened Al-Cu-Mg/Li, Metall Mater Trans A, 38A (2007) 3042-3062.
[64] Y. Ro, S.R. Agnew, R.P. Gangloff, Environmental exposure dependence of low growth rate fatigue crack damage in Al-Cu-Li/Mg alloys, in: J.E. Allison, J.W. Jones, J.M. Larsen, R.O. Ritchie (Eds.) Fourth International Conference on Very High Cycle Fatigue, TMS-AIME, Warrendale, PA, 2007, pp. 407-420.
[65] R.J.H. Wanhill, Corrosion Fatigue of Aircraft Materials, AGARD Report No. 659, in, North Atlantic Treaty Organization, Neuilly Sur Seine, France, 1977, pp. 2-1 to 3-37.
[66] F.J. Bradshaw, C. Wheeler, Applied Materials Research, 5 (1966) 112-120.
[67] R.P. Gangloff, Hydrogen asisted cracking of high strength alloys, in: J. Petit, P. Scott (Eds.) Comprehensive Structural Integrity: Environmentally Assisted Fracture, Elsevier, New York, NY, 2003, pp. 31-101.
[68] R.P. Gangloff, in: N.R. Moody, A.W. Thompson, R.E. Ricker, G.W. Was, R.H. Jones (Eds.) Hydrogen Effects on Material Behavior and Corrosion Deformation Interactions, The Minerals, Metals & Materials Society, Warrendale, PA, 2003, pp. 477-497.
[69] W.H. Hartt, J.S. Tennant, W.C. Hooper, in: H.L. Craig, T.W. Crooker, D.W. Hoeppner (Eds.) Corrosion Fatigue Technologies, ASTM STP 642, ASTM International, West Conshohocken, PA, 1978, pp. 5-18.

[70] R.J. Taunt, W. Charnock, Fluid Compositions within Fatigue Cracks, Mater Sci Eng, 35 (1978) 219-228.
[71] A. Turnbull, A Theoretical Evaluation of the Influence of Mechanical Variables on the Concentration of Oxygen in a Corrosion Fatigue Crack, Corros Sci, 22 (1982) 877-893.
[72] A. Turnbull, Theoretical-Analysis of Influence of Crack Dimensions and Geometry on Mass-Transport in Corrosion-Fatigue Cracks, Mater Sci Tech Ser, 1 (1985) 700-710.
[73] A. Turnbull, in: R.M. Latanision, R.H. Jones (Eds.) Chemistry and Physics of Fracture, Martinus Nijhoff Publishers, AD Dordrecht, Netherlands, 1987, pp. 287-310.
[74] A. Turnbull, Modeling of the chemistry and electrochemistry in cracks - A review, Corrosion, 57 (2001) 175-189.
[75] Thermopedia, in.
[76] E.L. Cussler, Diffusion, mass transfer in fluid systems, Cambridge University Press, Cambridge Cambridgeshire ; New York, 1984.
[77] T.I. Gombosi, Gaskinetic theory, Cambridge University Press, Cambridge England ; New York, 1994.
[78] J. Kestin, K. Knierim, E.A. Mason, B. Najafi, S.T. Ro, M. Waldman, Equilibrium and Transport-Properties of the Noble-Gases and Their Mixtures at Low-Density, J Phys Chem Ref Data, 13 (1984) 229-303.
[79] T.L. Anderson, Fracture Mechanics : Fundamentals and Applications, CRC Press, Boca Raton, FL, 1991.
[80] B.P. Somerday, P. Sofronis, K.A. Nibur, C. San Marchi, R. Kirchheim, Elucidating the variables affecting accelerated fatigue crack growth of steels in hydrogen gas with low oxygen concentrations, Acta Mater, 61 (2013) 6153-6170.
[81] S. Lynch, Acta Metallurgica, 36 (1988) 2639-2661.
[82] J.S. Warner, S. Kim, R.P. Gangloff, Molybdate inhibition of environmental fatigue crack propagation in Al-Zn-Mg-Cu, Int J Fatigue, 31 (2009) 1952-1965.

Figures:

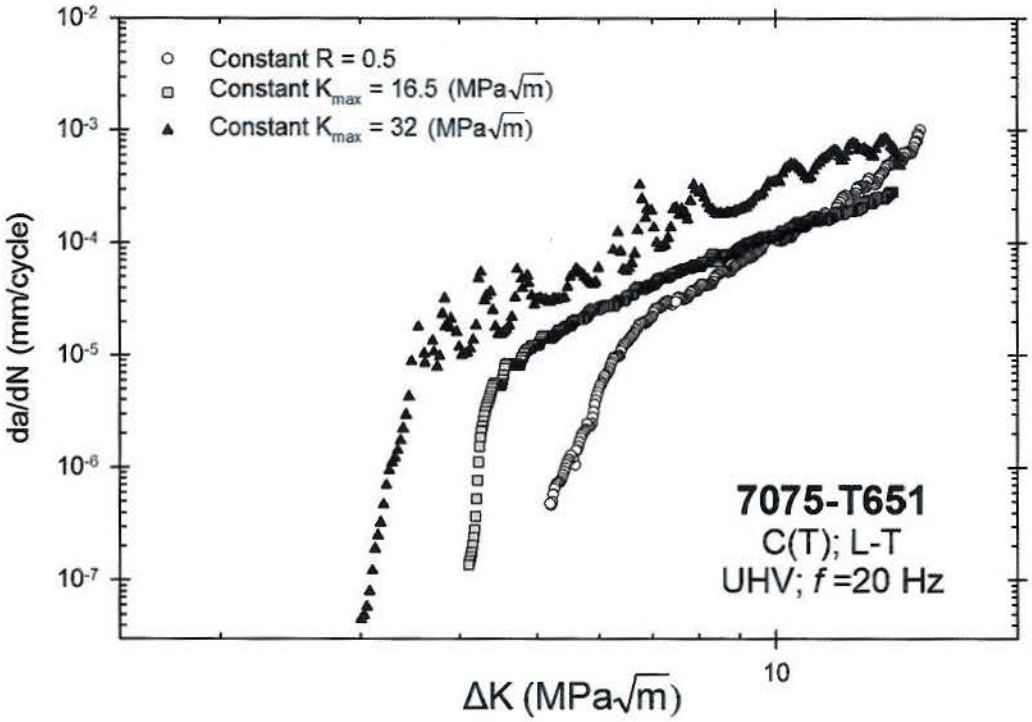

Figure 1: Effect of loading format and R value on da/dN versus ΔK for 7075-T651 (L-T orientation) stressed in ultra-high vacuum with P_{H2O} = 0.25-0.5 μPa.

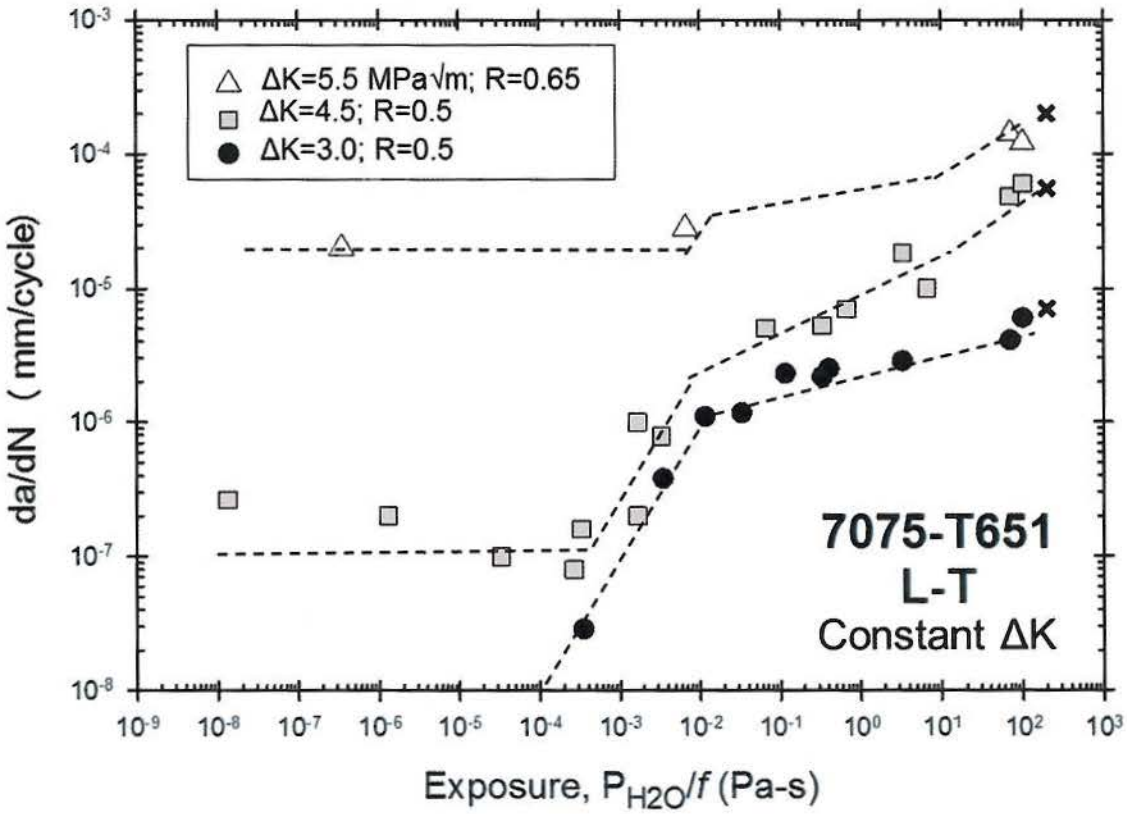

Figure 2: Effect of high purity water vapor exposure parameter on fatigue crack growth rate in 7075-T651 (L-T) stressed at constant ΔK of 3.0 and 4.5 MPa√m (constant R = 0.5) and at ΔK of 5.5 MPa√m (R = 0.65). Results for FCP in this lot of 7075-T651 stressed in moist air are given by (**x**).

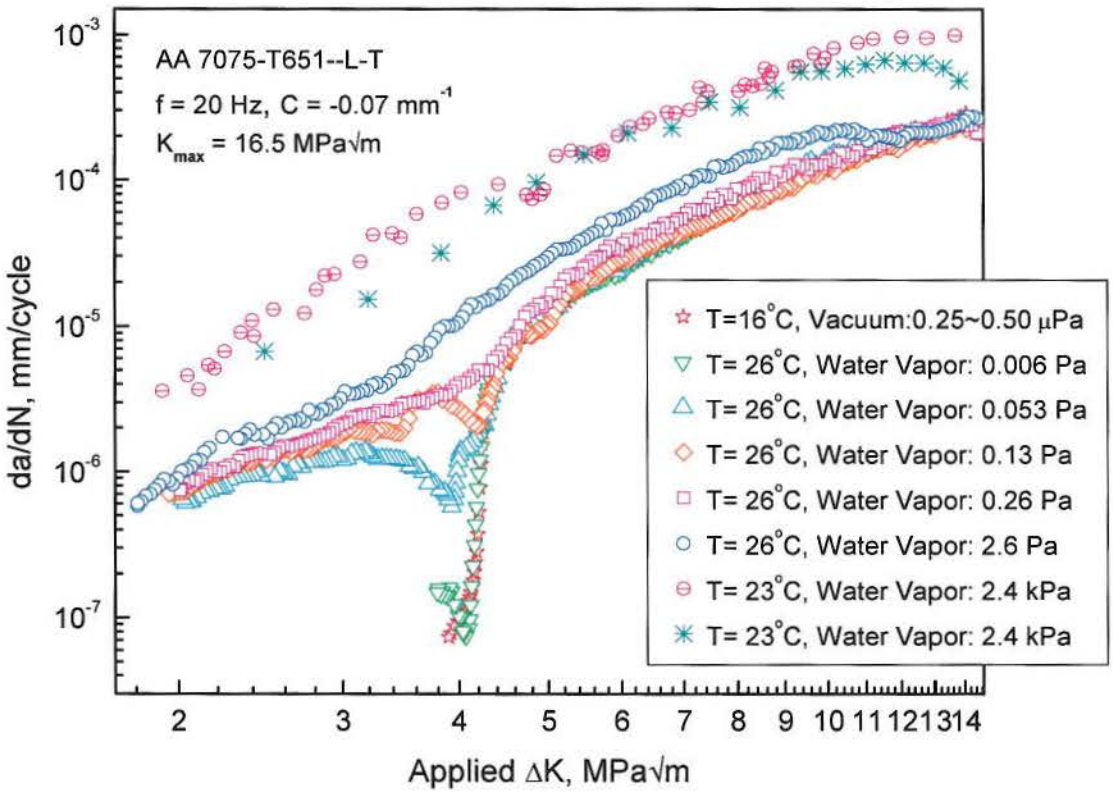

Figure 3: Fatigue crack growth rate versus decreasing ΔK at constant K_{max} of 16.5 MPa√m (f = 20 Hz) for 7075-T651 (L-T) at various-constant water vapor pressures from UHV (0.25 to 0.50 μPa) to 2.4 kPa.

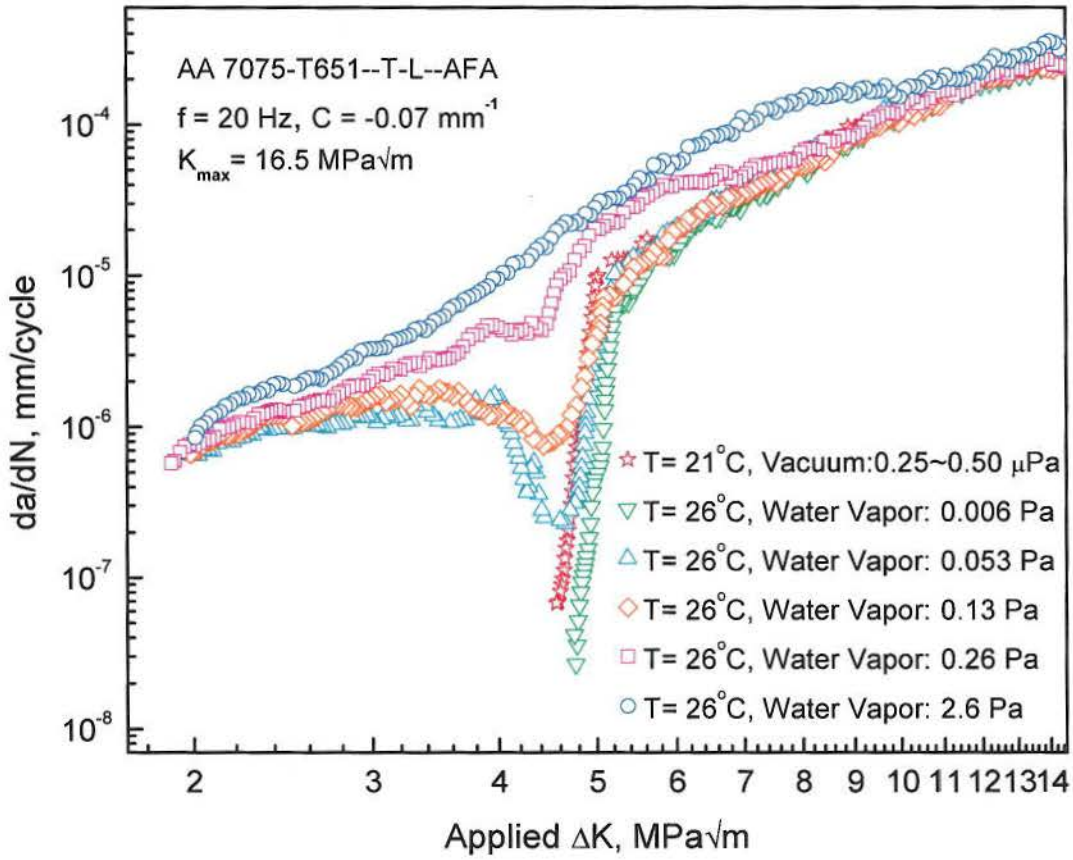

Figure 4: Fatigue crack growth rate versus decreasing ΔK at constant K_{max} of 16.5 MPa√m (f = 20 Hz) for 7075-T651 (T-L) at various-constant water vapor pressures from UHV (0.25 to 0.50 μPa) to 2.6 Pa.

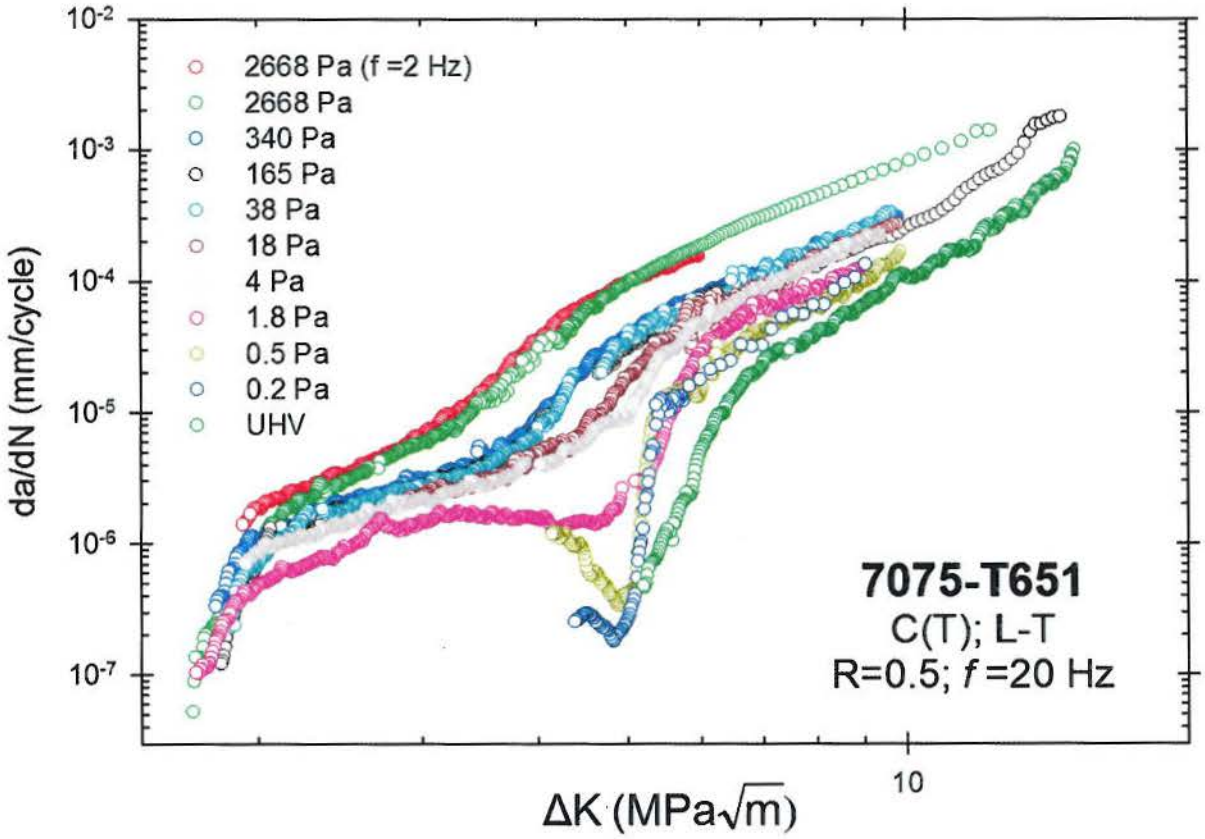

Figure 5: Fatigue crack growth rate versus decreasing ΔK at constant R of 0.50 (f = 20 Hz) for 7075-T651 (L-T) at various-constant water vapor exposure levels from ultra-high vacuum (0.25-0.50 μPa-s) to 1.3 kPa-s (P_{H2O} = 26.7 kPa).

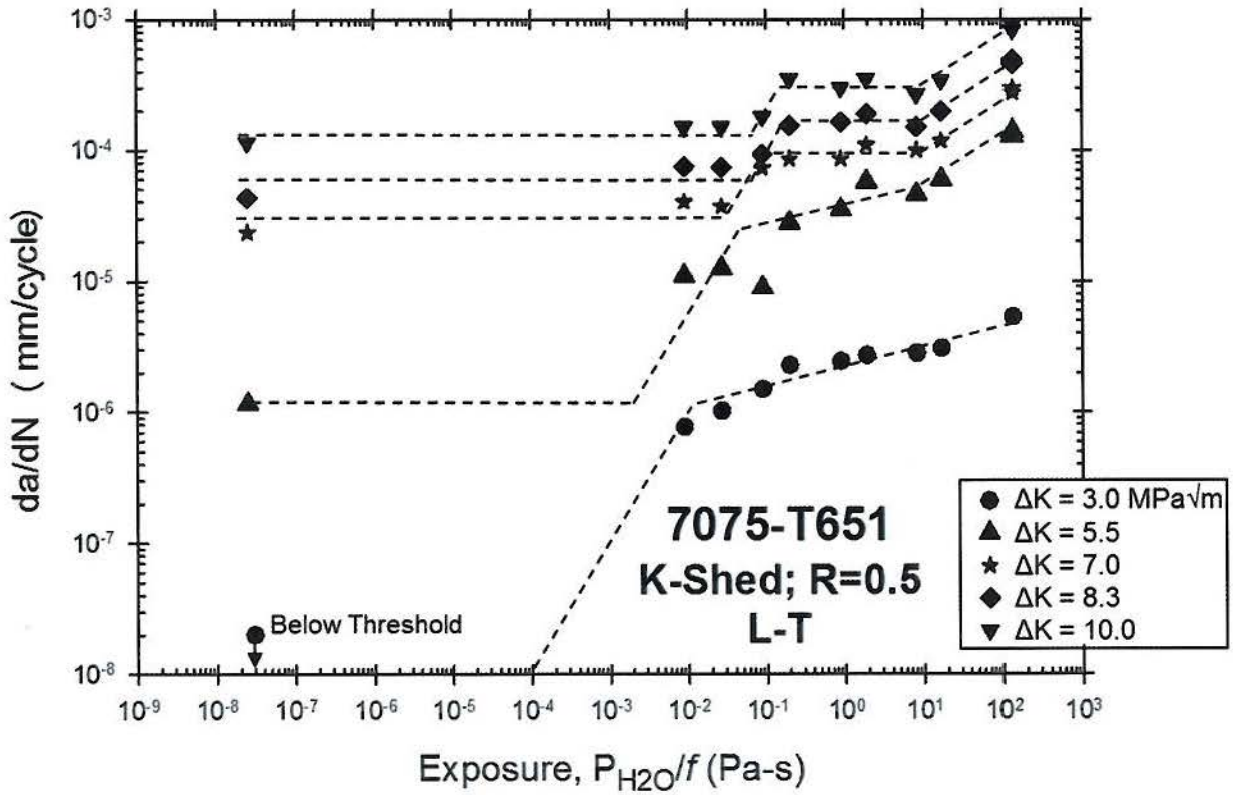

Figure 6: Effect of high purity water vapor exposure parameter on fatigue crack growth rate in 7075-T651 (L-T) stressed at various-constant ΔK levels, each at fixed R of 0.50 and f = 20 Hz, taken from the wide-range decreasing ΔK data in Figure 5.

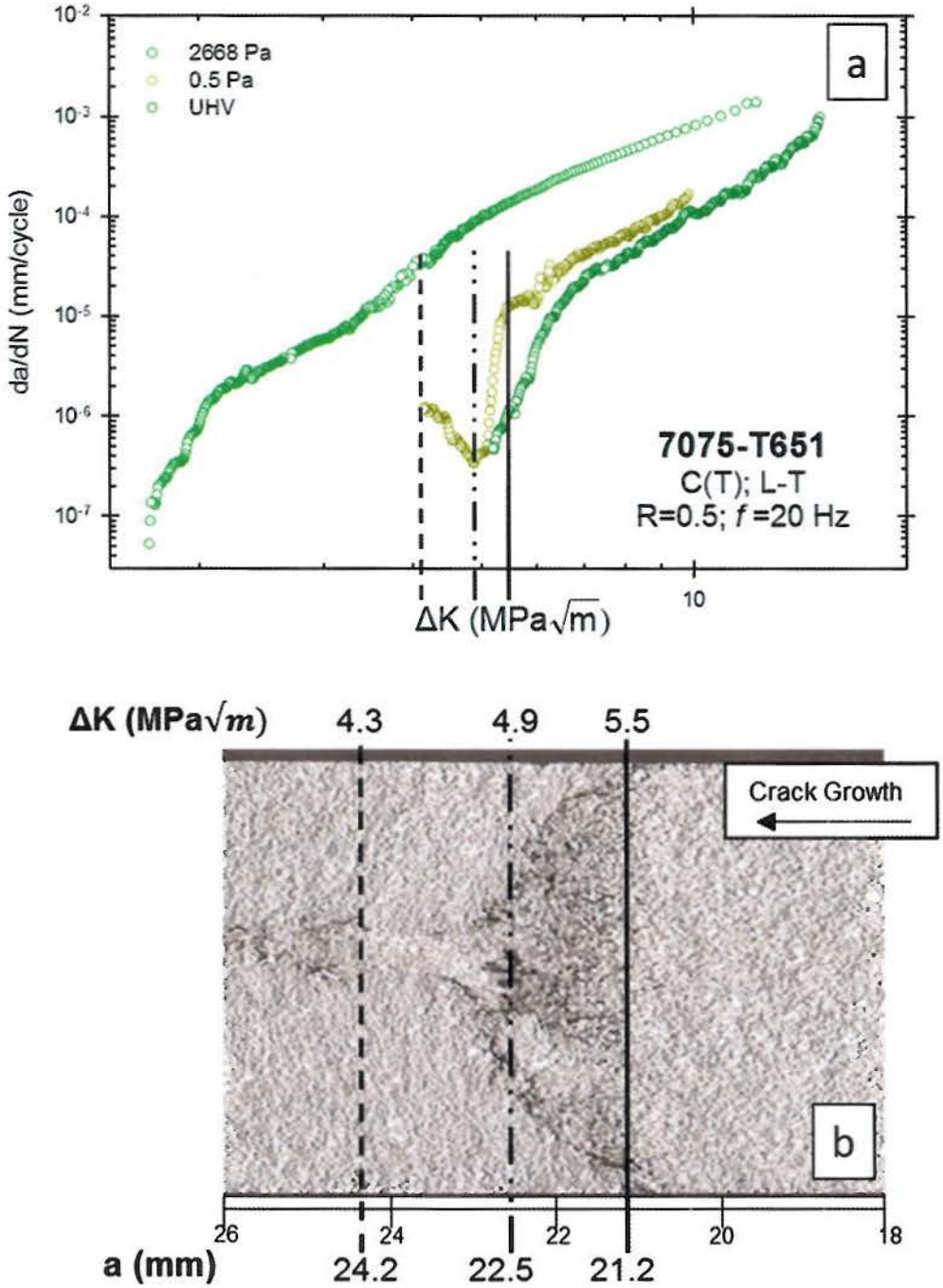

Figure 7: Crack growth rate versus ΔK (a) and corresponding optical fractograph (b) illustrating the transition from macroscopically smooth to rough topography on the fatigue crack surface of 7075-T651 (L-T orientation) stressed in pure water vapor at P_{H2O} = 0.5 Pa. For constant R, ΔK decreased with increasing crack length from right to left in this image.

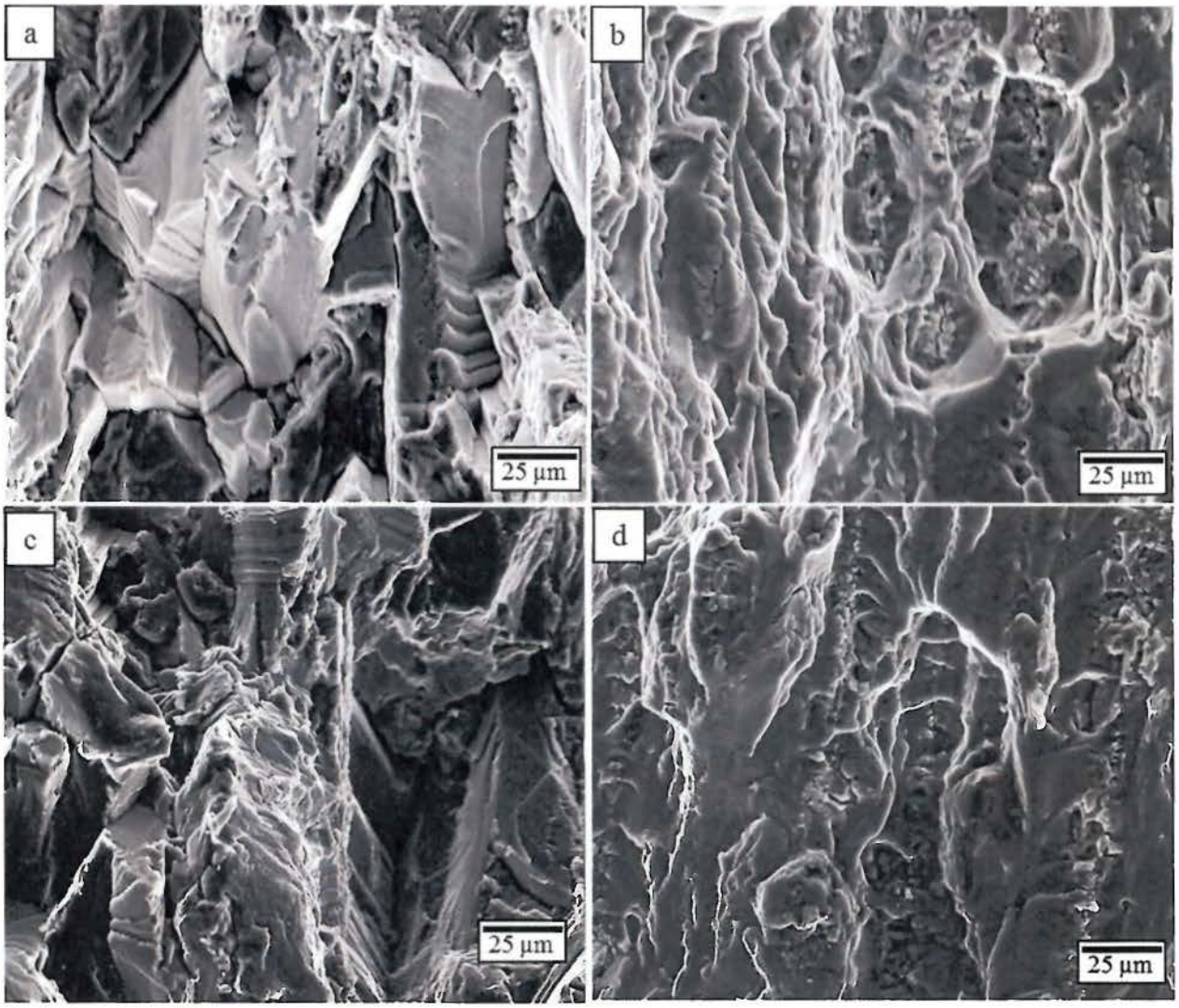

Figure 8: SEM images of the fatigue crack surface of 7075-T651 tested in UHV at f = 20 Hz and constant K_{max} = 16.5 MPa√m for a T-L oriented specimen at ΔK of: (a) ~4.3 and (b) ~12.7 MPa√m, as well as for a L-T oriented specimen at ΔK of (c) ~5.0 and (d) ~12.9 MPa√m. Crack growth is from bottom to top in each image.

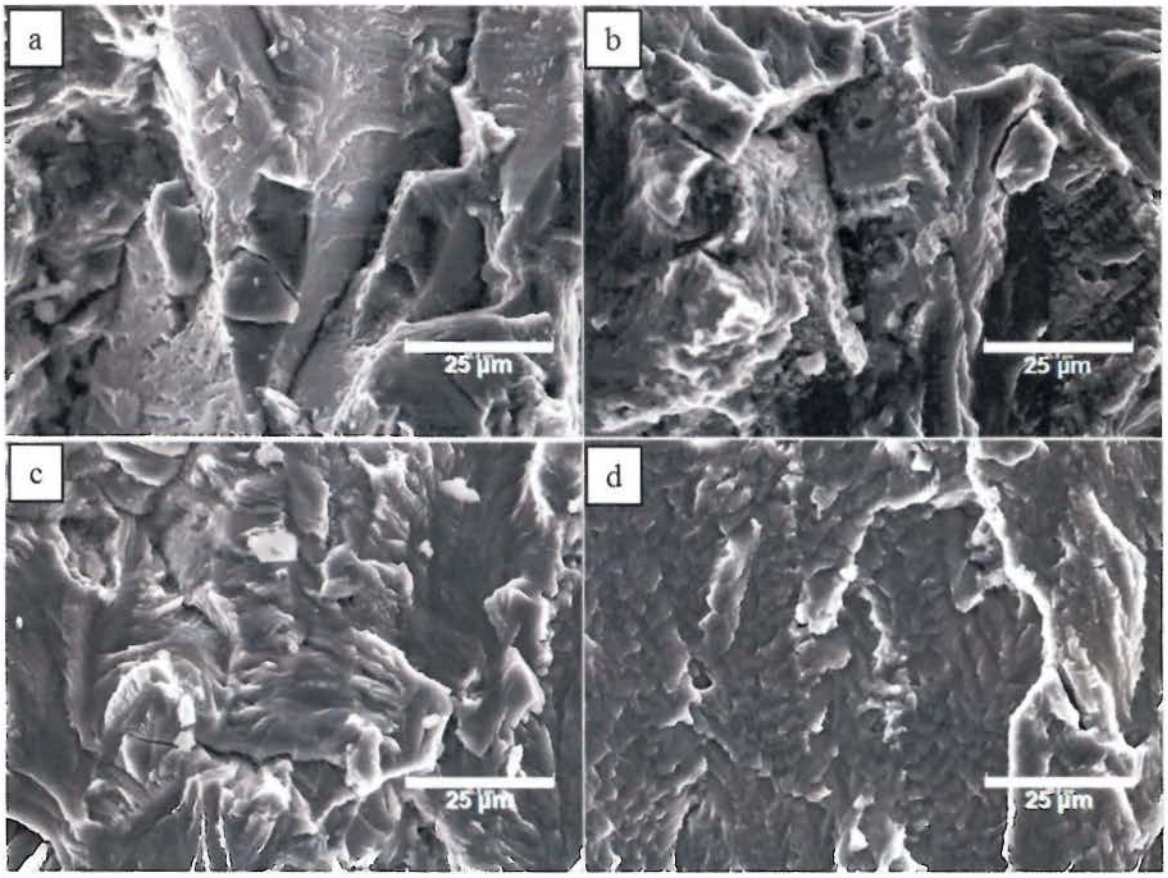

Figure 9: SEM images of the fatigue crack surface of 7075-T651 tested at constant R = 0.5, f = 20 Hz and constant ΔK = 4.5 MPa√m (from Figure 1) for an L-T oriented specimen exposed to P_{H2O} of: (a) 0.007, (b) 0.066, (c) 6.6 and (d) 1,400 Pa. Crack growth is from bottom to top in each image.

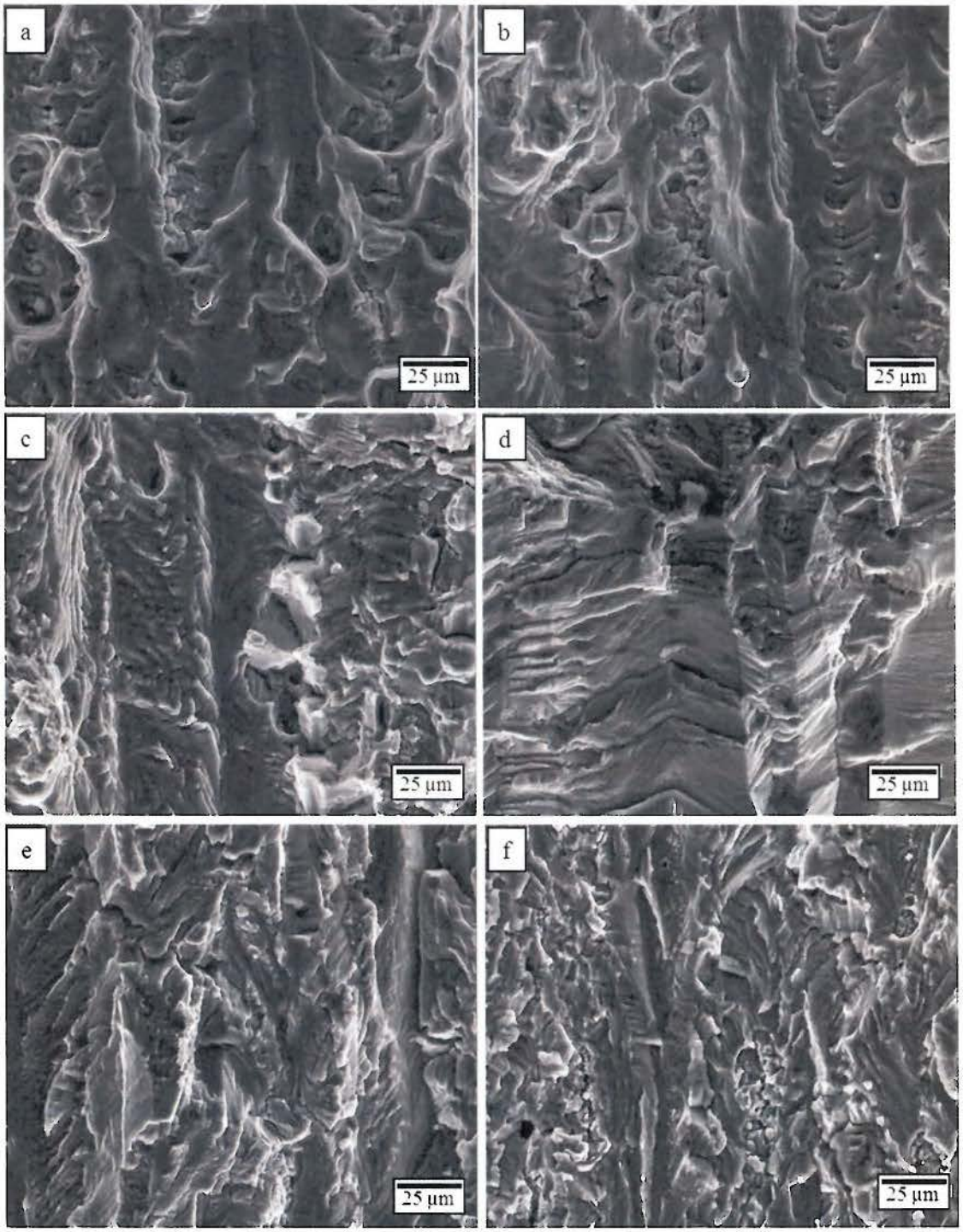

Figure 10: SEM images of the fatigue crack surface of 7075-T651 tested at P_{H2O} = 0.13 Pa, f = 20 Hz and constant K_{max} = 16.5 MPa√m for a T-L oriented specimen with ΔK of: (a) ~12.5, (b) ~6.7, (c) ~5.4, (d) ~4.5, (e) ~3.3 and (f) ~2.2 MPa√m. Crack growth is from bottom to top in each image.

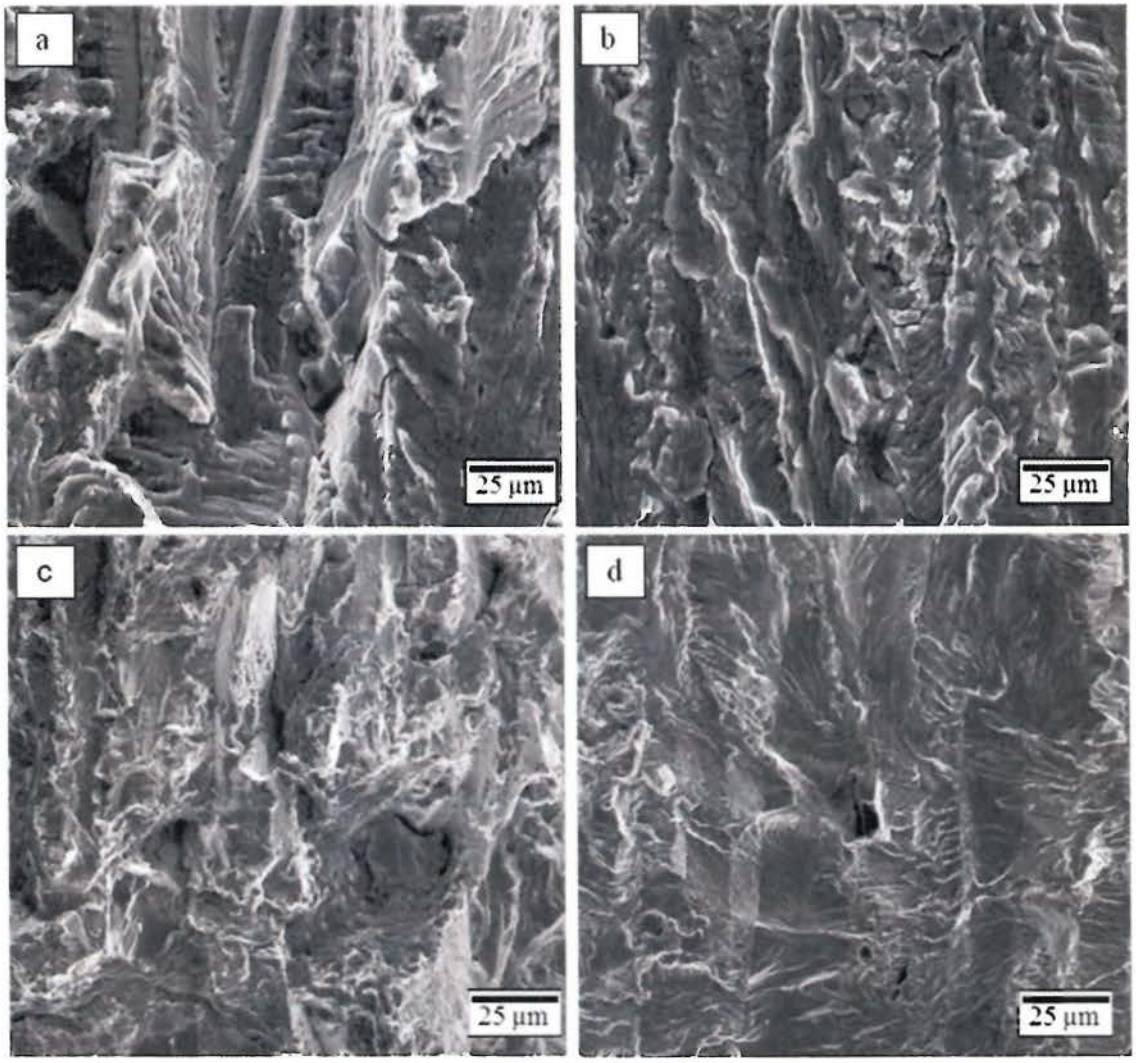

Figure 11: SEM images of the fatigue crack surface of 7075-T651 tested under decreasing ΔK loading at f = 20 Hz for: (a) and (b) constant K_{max} (16.5 MPa√m, T-L) with ΔK of (a) ~4.8 and (b) ~2.4 MPa√m with P_{H2O} = 0.053 Pa; and (c) and (d) constant R (0.5, L-T) with ΔK of: (c) ~5 and (d) ~3.0 MPa√m with P_{H2O} = 0.5 Pa. The direction of crack growth is from top to bottom.

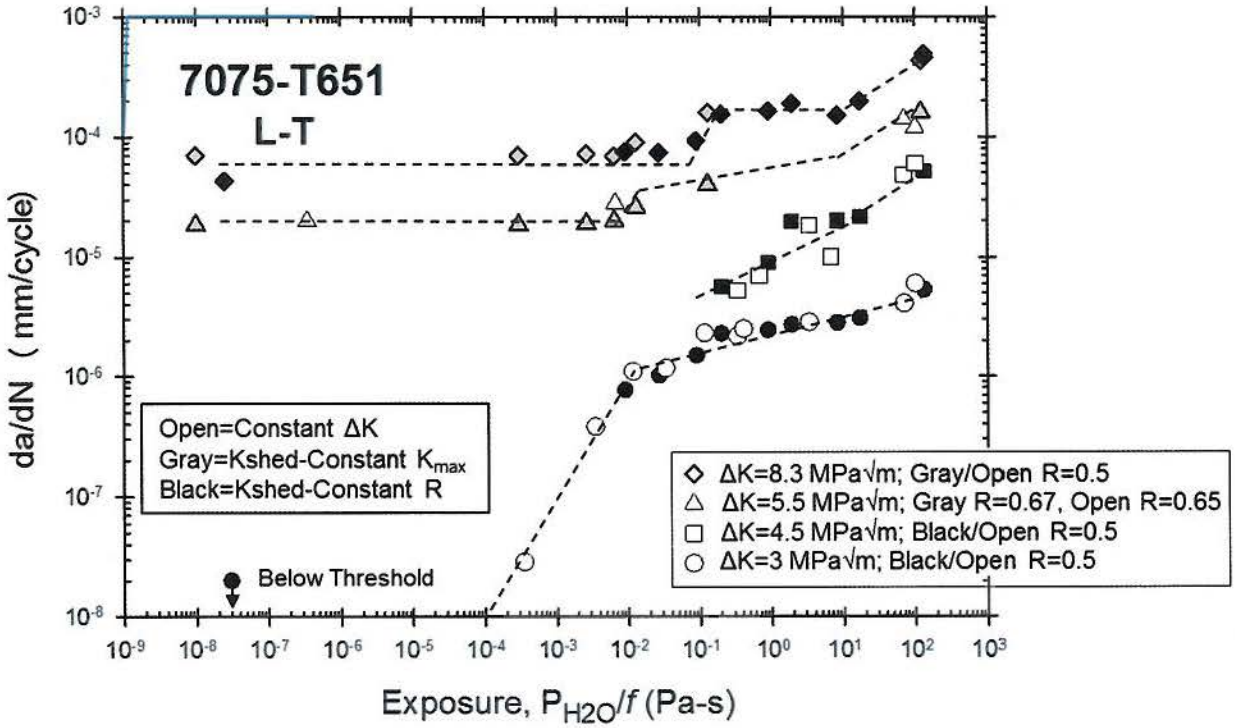

Figure 12: Effect of water vapor exposure on crack growth rate for 7075-T651 (L-T orientation) at ΔK levels of 3.0, 4.5 and 5.5 MPa√m, as established by (a) either constant ΔK-constant R (0.5) loading (Figure 1, open symbols), (b) constant K_{max} (16.5 MPa√m)-decreasing ΔK loading (Figure 2; gray symbols), or (c) constant R (0.5)-decreasing ΔK loading (Figure 4; black symbols).

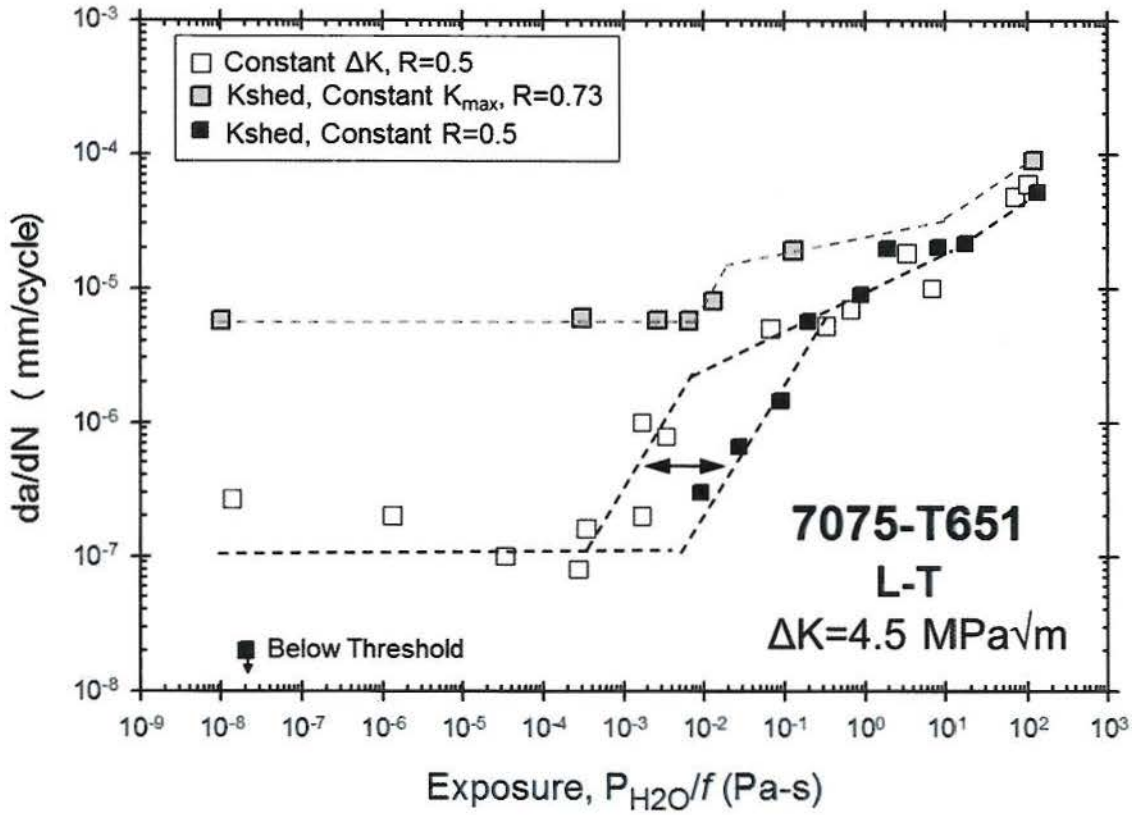

Figure 13: Effect of water vapor exposure parameter on crack growth rate for 7075-T651 (L-T) at ΔK of 4.5 MPa√m, established by either: (a) constant ΔK-constant R (0.5) experiments (Figure 1, □), (b) constant K_{max} (16.5 MPa√m)-decreasing ΔK loading (Figure 2, ■), or (c) constant R (0.5)-decreasing ΔK loading (Figure 4, ■).

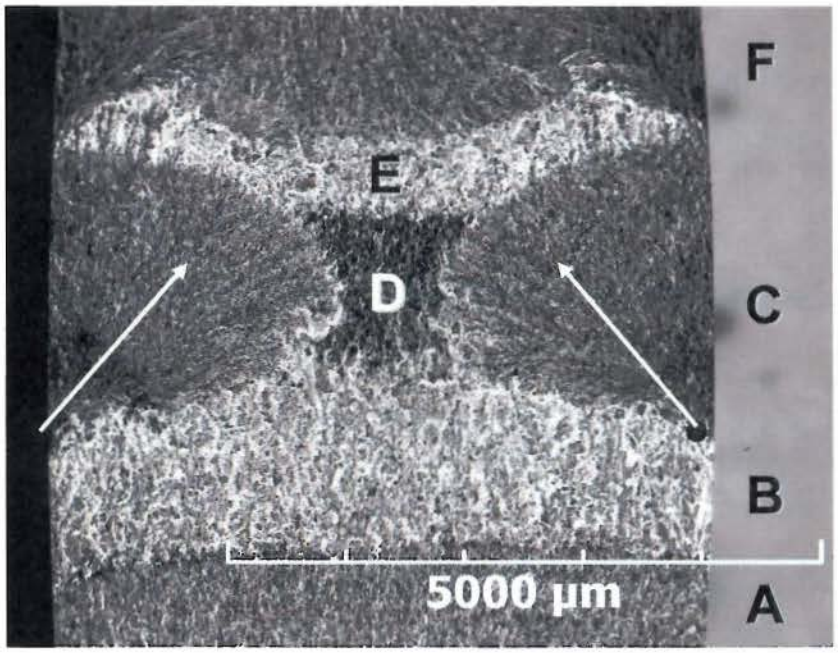

Figure 14: SEM image of a CT specimen of 7075-T651 loaded at $f = 20$ Hz, constant $\Delta K = 4.5$ MPa$\sqrt{m}$ and $R = 0.5$ showing the irregular crack front shape caused by P_{H2O}/f change. Regions A, C, and F represent high water vapor pressure exposure, whereas regions B, D, and E represent very low P_{H2O}. The specimen thickness is horizontally oriented and the Mode I crack growth direction is from bottom to top.

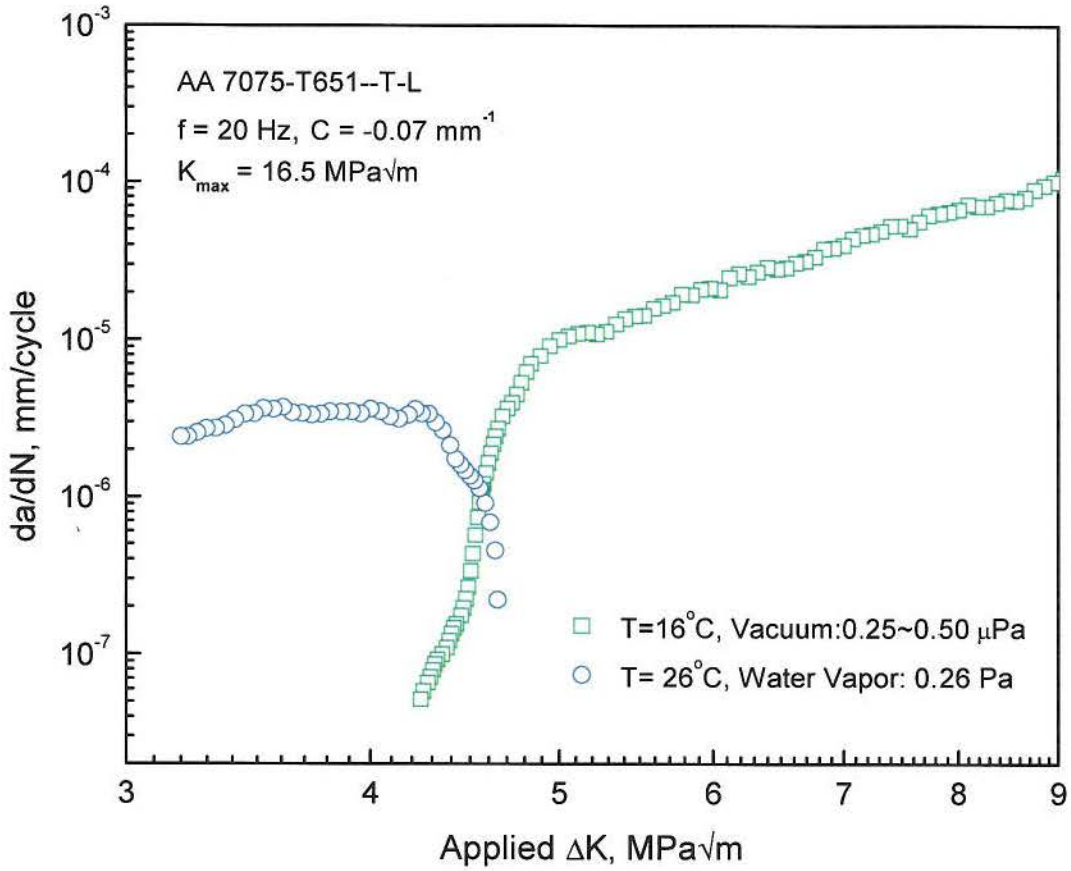

Figure 15: Crack growth rate response for 7075-T651 (T-L), which was fatigue cracked under decreasing ΔK and constant K_{max} (16.5 MPa√m) in UHV to near ΔK_{TH}, followed by introduction of 0.26 Pa water vapor and continued decreasing ΔK loading with the identical constant K_{max}. Crack growth rate was essentially 0 for the first 20 h of this loading in water vapor, followed by the rising da/dN with declining ΔK.

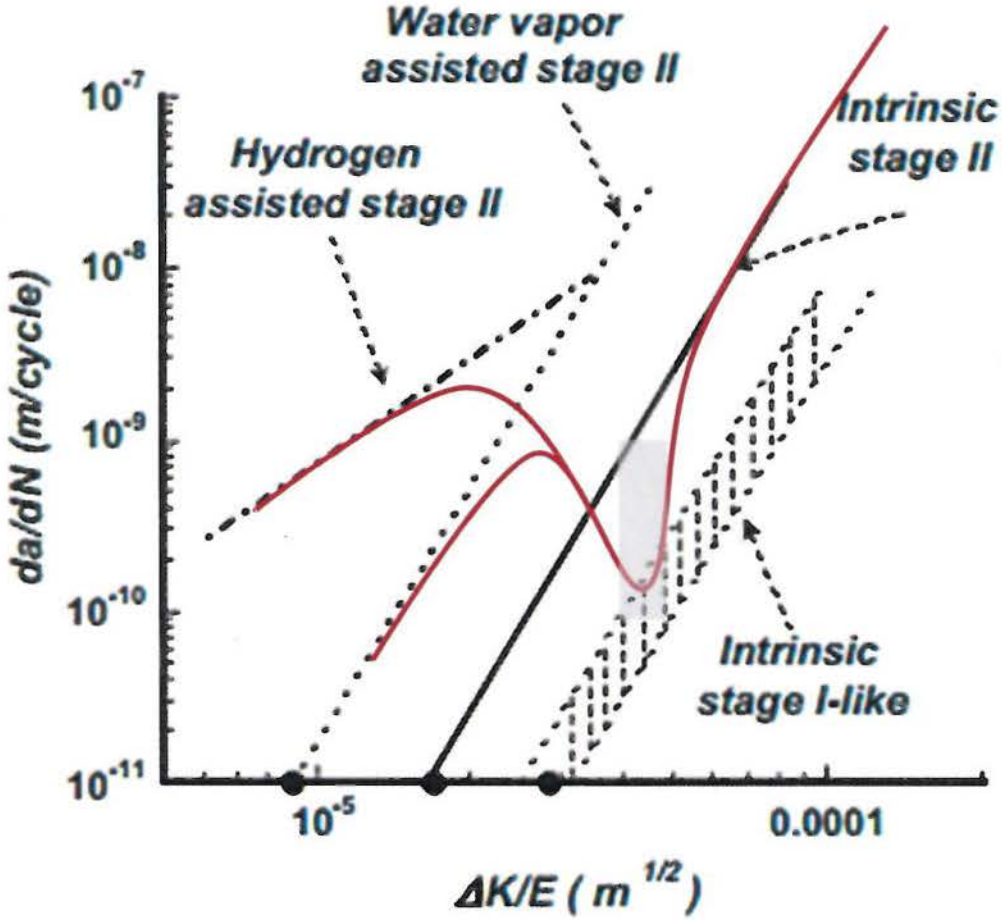

Figure 16: Schematic diagram showing the dependencies of fatigue crack growth rate on the modulus-normalized closure-free stress intensity range, as governed by crack tip plasticity for an inert environment (intrinsic Stage I and Stage II) and environment enhanced crack tip damage due to an adsorbate or H. (After Petit and co-workers).

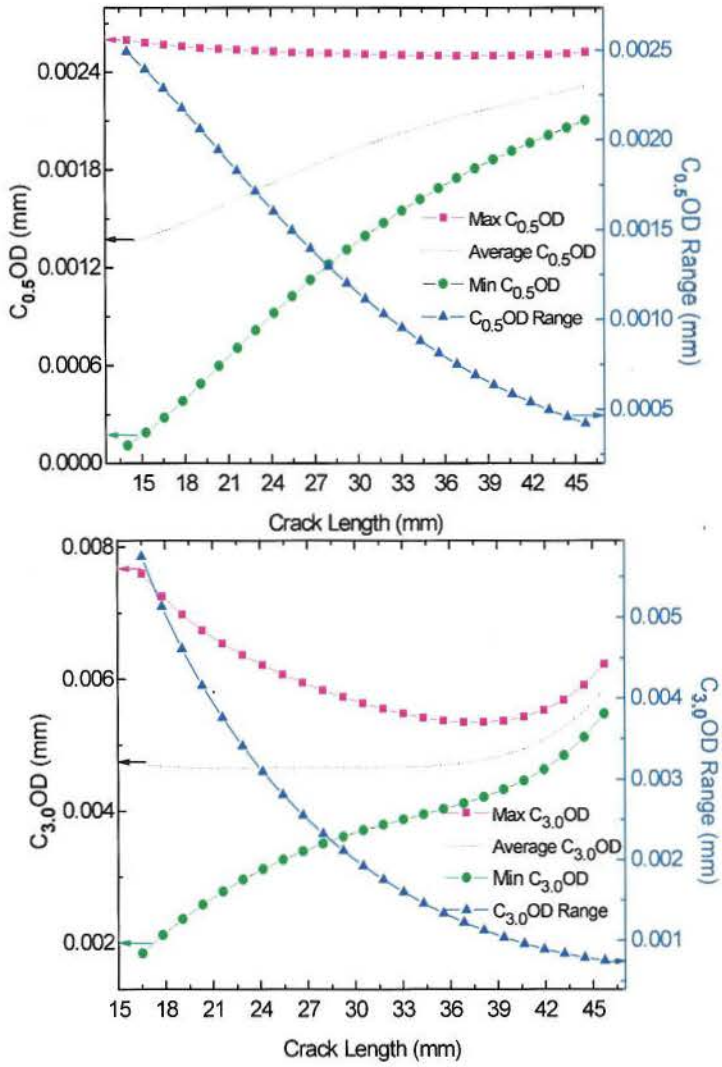

Figure 17: Calculated crack tip opening displacements versus crack length for constant K_{max} loading of 7075-T651 with C = -0.07 mm^{-1}. Plotted values include elastically estimated maximum, minimum, range and per-cycle average values of COD.